Density functional theory of interacting hard spheres: The formation of complex Frank-Kasper phases

By Yu Li, B. Sc. (Honours)

A Thesis Submitted to the School of Graduate Studies in the Partial Fulfillment of the Requirements for the Degree Master of Science

Lay Abstract

Soft condensed matter physics, a sub-field of condensed matter physics, primarily concerns the investigation of physical properties of pliable, deformable materials such as plastics, gels, and colloidal suspensions. One particularly intriguing feature of these soft materials is their ability to self-assembly, leading to the spontaneous formation of ordered structures, including but not limited to body-centered cubic and face-centered cubic phases. In particular, a group of complex spherical phases, known as the Frank-Kasper phases, has been identified in various soft matter systems, encompassing polymeric blends, colloidal suspensions, and more. Notably, in colloidal systems, when nanoparticles are grafted with polymer chains, the Frank-Kasper phases could become stable. However, the emergence of these complex phases from the diverse soft matter systems have not been fully understood. In this thesis, we employ the classical density functional theory based on three different hard-sphere models to probe the formation of the Frank-Kasper phases in colloidal systems. Our results provide insights into the formation mechanism of the Frank-Kasper phases in a simple system and demonstrate the universality of different hard-sphere models.

Abstract

Understanding the phase behaviour of colloidal systems is relevant to designing new colloid-based nanostructured materials. One common platform for studying the colloidal system is the model of hard spheres. Over the last few decades, different hard-sphere models have been developed. We study the phase behaviour of three hard-sphere models: the lattice gas model, the local density approximation model, and the white bear version of the fundamental measure theory, with short-range attractive and long-range repulsive (SALR) interactions. The competition between the attraction and repulsion results in the formation of clusters composed of many particles, whereas the spatial arrangement of these clusters leads to the formation of long-range ordered phases. Phase diagrams containing the commonly observed body-center-cubic (BCC) and hexagonally close-packed (HCP) phases, as well as the novel Frank-Kasper σ and A15 phases, have been constructed using the density functional theory applied to hard spheres with SALR interactions. Similar phase transition sequences have been predicted for the three hard-sphere models, implying a universality of the observed phase behaviour for hard spheres interacting with SALR potentials. However, the details of the phase diagrams could vary significantly. The results obtained from our study shed light on understanding the emergence of complex phases from simple systems.

Acknowledgements

I would like to profoundly express my gratitude to my supervisor, Dr. An-Chang Shi, for his unwavering support, invaluable guidance, and constant encouragement throughout my graduate studies. His guidance helped me at all times during my research and writing of this thesis. I could not have imagined having a better mentor for my research. I am grateful to my colleagues: Mr. Jiayu Xie, for his dedicated efforts and the time he spent on this project; Mr. Yang Yang, for the inspiration and the enjoyable fishing excursions we shared over the past two years, as well as to Ms. Desiree Rehel, for the time and effort she spent on proofreading my thesis. My heartfelt thanks go to the members of my supervisory committee: Dr. Kari Dalnoki-Veress and Dr. Robert Wickham for the commitment and the time they spent on my committee meetings and reviewing this thesis. I extend my deepest gratitude to my parents and other family members for their indispensable financial and emotional support. Without their assistance, reaching this milestone would have been unattainable.

Contents

List of Figures

List of Tables

Declaration of Contribution

I designed two SALR potentials and constructed six phase diagrams for three different hard-sphere models as part of my research. I carried out all the theoretical analyses. The majority of the computation code was developed by my colleague, Mr. Jiayu Xie, which I also adapted to meet our research requirements. For the theoretical derivation of the lattice gas model, as well as the introduction to the preconditioned conjugate gradient method in Chapter 2 and numerical solution details in Appendix A, I closely followed Mr. Xie's notes. While I wrote this thesis, it was reviewed and edited by both me and Dr. An-Chang Shi. Dr. Shi provided the original idea and guided me toward the main results of this thesis.

Chapter 1

Introduction

The term "soft matter" is used to describe a range of materials characterized by their soft and deformable nature. This field encompasses both macroscopic entities, such as plastic product and non-Newtonian fluids like silly putty, as well as macromolecules, including DNA and RNA. Soft condensed matter physics investigates the collective behaviors of nano particles, typically ranging in size from 1 nanometer to 1 micrometer. The typical soft matter systems include, but are not limited to, polymeric systems, colloidal suspension, biological systems, and liquid crystals [21]. Owing to the self-assembly properties intrinsic to soft matter systems, they can spontaneously form ordered structures, and thereby display complicated phase behaviors. The cornerstone to understanding this phenomenon is the concept of frustration. In condensed matter physics, systems are "frustrated" when they are unable to simultaneously optimize competing interactions [30, 47, 48]. For instance, in block copolymer systems, hydrophobic and hydrophilic properties are simultaneously present on the same copolymer chain. Especially in diblock polymer systems, the copolymer chain typically contains A-type and B-type monomers, which repel each other. To minimize the free energy and avoid unfavorable contact,

the polymer systems tend to form A-rich and B-rich domains, exhibiting micro-phase separation [26]. Even for star-like dendrimer systems, which are modeled as ultra-soft spheres with a purely repulsive intermolecular potential, cluster crystal structures can form [29]. In contrast to crystalline solids, where each lattice site is occupied by a single atom, numerous nanoparticles can adhere together, forming clusters that occupy these lattice sites, thereby creating what is known as cluster crystals. Likos *et al.* showed that the formation of cluster crystals in ultra-soft sphere systems is mainly determined by the Fourier transform of the intermolecular interactions $V(k)$ [20, 29]. Ultra-soft sphere can form cluster crystals at arbitrary temperatures if $V(k)$ oscillates around zero (known as $Q^{\pm}$ potential) and the density is high enough. This is because the negative Fourier components of $V(k)$ reduce the free energy when the system form crystal structures. Meanwhile, such a system can remelt at high density if $V(k)$ only has non-negative Fourier components [1, 20]. Another important class of the soft matter is colloidal systems, which include polymer-grafted metal particles, charged nanoparticles, etc. In theoretical studies, colloidal systems are usually treated as hard-core spheres covered by soft coronas [38]. Colloidal systems can form solid phases such as body-centered cubic (BCC), face-centered cubic (FCC), and body-centered tetragonal (BCT) [28]. Besides these classical structures, more exotic phases, such as the Laves C14 phase, have also been observed in experiments [34].Their ability to cluster has been used as a new method for synthesizing exotic structures, and therefore, it has attracted significant attention in the soft matter community [33, 34, 38]. In cluster crystals, the inter-particle interaction is described by a short-range attractive and long-range repulsive potential (SALR), representing a combination of depletion force and electrostatic interaction in colloid suspensions. A competition between the

attractive and repulsive parts can suppress the gas-liquid transition, leading to clustering. The basic idea of cluster crystal is illustrated in 1.1.The short-range attractive part promotes the clustering process, while the repulsive tail limits the size of clusters. These clusters can further form periodic structures. In theoretical studies, such hard-sphere systems have demonstrated abundant cluster phase behaviors, including classical spherical structures, hexagonal structures, double gyroid structure, lamellar structures, and inverted structures [38, 49]. Besides these classical phases, a type of complex spherical phase, named the Frank-Kasper phases, has been discovered in copolymer and colloidal systems in both experimental and theoretical studies [22, 23, 34, 56, 58, 63].

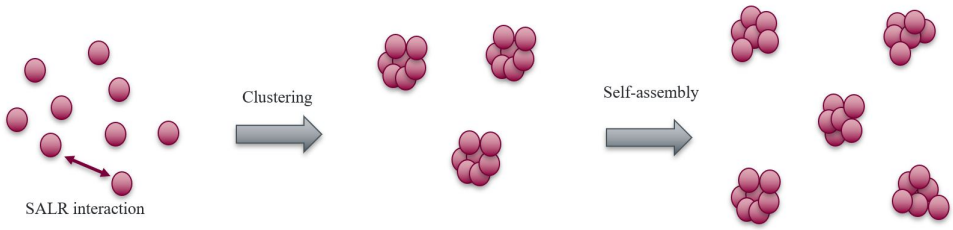

FIGURE 1.1: The basic idea of forming hard-particle cluster crystals is illustrated above. The SALR interaction promotes the formation of finite-size clusters. The cluster can form cluster crystal via self-assembly.

1.1 Origin of Frank-Kasper phases

The Frank-Kasper (FK) phases, also known as tetrahedrally close-packed phases, are widely found in metallic alloys. In 1958, F.C. Frank and J.S. Kasper first proposed a general geometric method to describe these complex phases found in metallic alloys [9]. In recent years, it has been discovered that Frank-Kasper

phases also exist in soft matter, such as block copolymers and colloid suspensions. The length scale of Frank-Kasper phases is very broad, ranging from atomic size (metallic alloys) to mesoscopic size (copolymers).

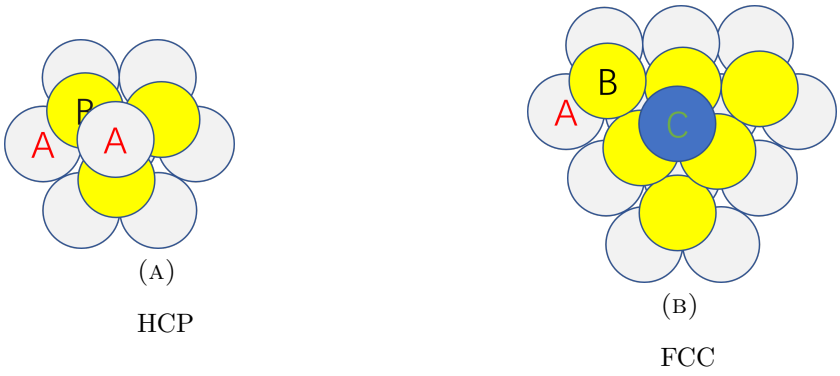

FIGURE 1.2: Illustration of two closed packing structures: Hexagonal closed packing (left) and Face centered cubic. They have the same packing density: $\rho = \frac{\pi}{3\sqrt{2}}$

In order to understand the formation of the Frank-Kasper phases, it is helpful to revisit a classical mathematical question: In three dimensions, how can we arrange identical hard spheres to achieve the maximum packing density? In the 17^{th} century, Johannes Kepler proposed his famous conjecture to answer this question: the face-centered cubic (FCC) and hexagonal close packing (HCP) of identical hard spheres yield the highest packing density. However, the formal proof of Kepler's conjecture took a long time. In 1953, Fejes Toth pointed out that finding the maximum packing density of all possible arrangements could be simplified to a finite number of calculations. Following the method proposed by Fejes Toth, Thomas Hales carried out a numerical calculation in 1998, which demonstrated that the maximum packing density of randomly packed spheres is about 0.64 [4]. In 2014,

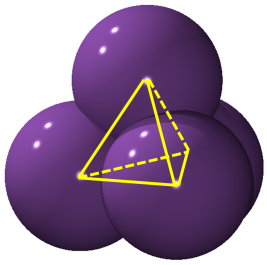

FIGURE 1.3: Four identical atoms are placed on the vertices of regular tetrahedron and give a simplest example of tetrahedrally close packing.

a collaborative project conducted by Hales was completed and provided a formal proof of Kepler's conjecture. Now, it has been proven that FCC and HCP give the maximum packing density: $\rho = \frac{\pi}{3\sqrt{2}}$, but with different way of stacking . Two ways of stacking are shown in Figure 1.2. The spheres in both structures are closely packed and have 12 nearest neighbors if all the spheres are identical.

A natural question arises: how does the packing pattern change if the spheres' volumes are not equal? An obvious fact is that the central atom and its 12 neighbors closely contact each other in FCC or HCP structure, but this becomes impossible if the thirteen atoms are not of the same size [9]. Frank and Kasper proposed an alternative way to arrange the thirteen atoms, placing the 12 neighboring atoms and the central atom on the vertices and center of an icosahedron, respectively [9]. If we connect the three nearest atoms on the icosahedron to the central atom, the four atoms are on the vertices of a nearly regular tetrahedron, and thus they are tetrahedrally close-packed. The tetrahedron is slightly deformed because a regular tetrahedron cannot fully fill up space. A simple example of a tetrahedrally closely-packed group is shown in Figure 1.3. Two advantages of tetrahedrally

closed packing are: (1) the central atom and neighboring atoms do not necessarily have to be the same size; (2) The atoms in the icosahedral grouping are equidistant from the central atom, and they do not necessarily touch their nearest neighbors, allowing more freedom for deformation [9]. These packing features are favored by systems containing multiple-sized atoms, such as metallic alloys and deformable micelle systems. However, due to the forbidden five-fold symmetry, the 12-fold icosahedral cannot fill the space and must be combined with other polyhedra. As a consequence, Kasper proposed other types of polyhedra, namely Kasper polyhedra, which are tetrahedrally close-packed and labeled by their coordination number: Z14, Z15, and Z16. These polyhedra are shown in Figure 1.4. If we connect the nearest neighboring atoms, the resulting coordination polyhedra only contain triangular faces. We also can connect the neighboring atoms (not only the nearest neighbors) to the central atom and construct planes bisecting these lines. The smallest volume enclosed by those planes is the Wigner-Seitz cell or Voronoi cells. Those cells can fill up the space without gaps and the periodic structures they formed are the Frank-Kasper phases.

Since the Frank-Kasper phases are tetrahedrally close-packed, one would expect them to be energetically favorable for systems containing multiple-sized atoms or mesoatoms. Indeed, at least 28 Frank-Kasper phases have been found in intermetallic alloys, and they are characterized by their mean coordination number [54]. However, there is no standard naming convention, and hence, we can find several names for the same Frank-Kasper phase in the literature. For instance, the C14 phase was first discovered in the $MgZn_2$ compound and is also called the $MgZn_2$ phase. Some Frank-Kasper phases are classified as classical Frank-Kasper

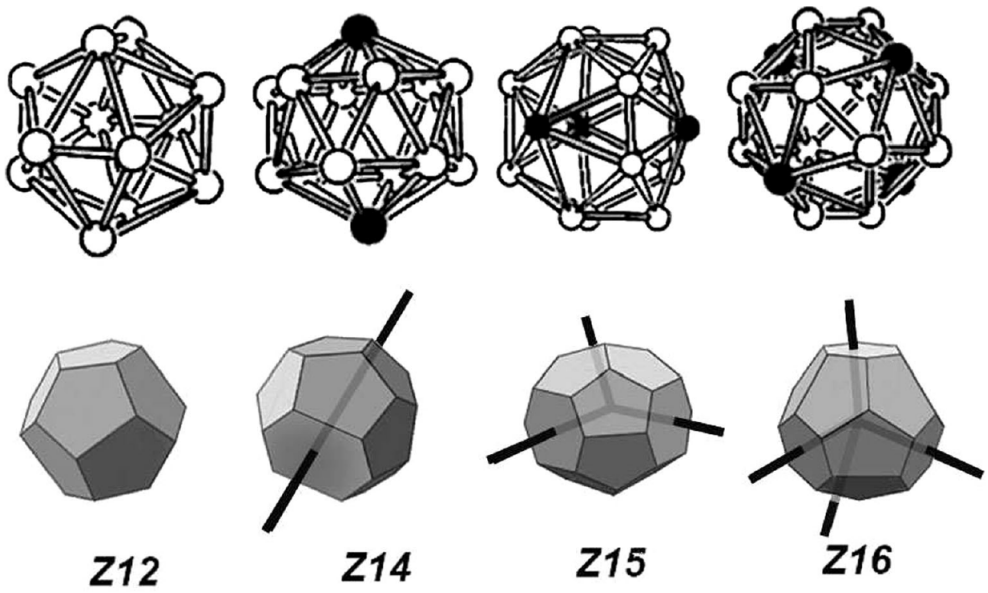

FIGURE 1.4: Four Frank-Kasper polyhedrons are plotted in the first row. The central atoms are not drawn. And the corresponding Voronoi cells of central atom are plotted in the second row. This figure is reprinted from reference [46].

phases, such as σ, A15, C14, C15, and others [54]. The letters are related to the composition of alloys: A stands for pure metal, C represents AB_2 compounds.

1.2 Frank Kasper phases in soft matter

The emergence of Frank-Kasper phases in soft matter systems, especially in diblock copolymer systems, has been studied extensively [16, 18, 56]. Experimentally, researchers have observed the σ and A15 phases in liquid crystalline dendrimers [3, 62], the C14 phase in polymer-grafted nanoparticles [10, 34], as well as the C14, C15, A15, and σ phases in concentrated surfactants [2, 17]. In general, a universal principle that describes the formation of Frank-Kasper phases in soft matter systems has not been developed. Fortunately, theorists have conducted some quantitative and qualitative analyses on the emergence of Frank-Kasper phases in diblock copolymer systems [17, 23, 40, 41, 51, 58]. Here, we consider the simplest diblock copolymer system containing only one type of AB diblock copolymer chain and assume A is the majority block. In the strong segregation regime, AB copolymer chains tend to form spherical micelles with cores mostly containing B blocks and shells containing A blocks to avoid unfavorable contact between A monomers and B monomers. Spherical micelles cannot fully fill up space, so the micelles have to deform, and their shapes become non-spherical. However, this deformation encounters resistance since it leads to an additional cost in interfacial energy between the core and shell, and loss of entropy due to the overstretching of chains. This conflict is called frustration, which originates from the competition between the deformation requirement and additional free energy penalty. The appearance of various Frank-Kasper phases in soft matter systems is the result of this frustration.

Milner and Olmsted developed the diblock foam model (DFM), which provides a quantitative measure of the interfacial energy and chain stretching of micelles [31, 32]. Later on, Reddy *et al.* used the DFM to study the formation of Frank-Kasper phases in diblock copolymer systems [41]. Here, we follow the argument of Reddy *et al.* and illustrate how Frank-Kasper phases become stable in copolymer systems. The free energy of a chain $F(X)$ can be expressed as a function of the packing parameter X, which represents a set of Voronoi cells of certain phases [41]:

$$F(X) = \gamma \frac{A(X)}{R_0} + \frac{\kappa}{2} I(X) R_0^2, \tag{1.1}$$

where γ and κ are constant related with chain properties. R_0 is the radius of a sphere which has the same volume to the mean volume of Voronoi cells V_i, and it is given by,

$$V = \frac{4\pi R_0^3}{3} = \frac{1}{n} \sum_{i=0}^{n} V_i, \tag{1.2}$$

where n is the number of Voronoi cells within one unit cell. And $A(X)$ measures the mean area of cell which is given by [32],

$$A(X) = \frac{1}{n} \sum_{i=0}^{n} A_i / (4\pi R_0^2).$$

Equation (1.1) has two contributions: the first term represents the interfacial energy between core and shell and hence it is proportional to the surface area; the second term represents the entropy due to stretching of the copolymer chain and $I(x)$ is the stretching moment which is defined as,

$$I(x) = \frac{1}{n} \sum_{i=0}^{n} I_i / (4\pi R_0^5 / 5), \tag{1.3}$$

where I_i is the second moment volume of Voronoi cells centered at $\vec{r}_i$:

$$I_i = \int d\vec{r} |\vec{r} - \vec{r}_i|^2. \tag{1.4}$$

Now we can calculate the free energy in equation (1.1) for different lattice structure X. For a perfect spherical cell, the free energy is,

$$F_0 = \frac{3}{2}(\gamma^2\kappa)^{\frac{1}{3}}. \tag{1.5}$$

For a ordered phase, the optimized R_0 gives the minimal free energy relative to F_0:

$$F(X) = F(X)_{R_0}/F_0 = \left[A^2(X)I(X)\right]^{\frac{1}{3}}. \tag{1.6}$$

Reddy *et al.* minimized the free energy over arbitrary volume and shape of cells for 11 Frank-Kasper phases, as well as for the FCC and BCC structures. Their study demonstrates that the optimal relaxation of Voronoi cells to unequal volumes minimizes area and maximizes the compactness of cells, which leads to the emergence of the Frank-Kasper phases [41]. As a consequence, their study confirms that the σ and A15 phases are stable in conformationally asymmetric diblock copolymer systems, in agreement with the SCFT predictions [58]. These studies emphasize that the space-filling requirement and free energy penalty of deformation are the key factors that promote the stabilization of Frank-Kasper phases in diblock copolymer systems. These two factors are also likely to be important for Frank-Kasper phases in other soft matter systems.

Colloidal particles are an important class of soft matter. In theoretical studies,

colloidal systems are described by hard core particles plus an inter-particle interaction. Combined with the mean field approximation of the inter-particle potential, the classical density functional theory (cDFT) is well-suited to describe such systems. Pini *et al.* constructed a phase diagram of hard core systems with a SALR potential by using cDFT [38, 39]. Their findings (Figure 1.5) suggest a generic phase transition sequence: classical spherical phases (BCC/HCP) → hexagonal (HEX) → double gyroid (DG) → lamella, and eventually to inverted phases (DG, HEX, BCC/HCP). The discovery of HCP and BCC phases indicates the likelihood of stabilizing Frank-Kasper phases in the region of spherical phases. Meanwhile, Dawson *et al.* studied the formation of A15 and σ phases by using Ginzburg-Landau theories[7]. They concluded that the stabilization of Frank-Kasper phases is more sensitive to the free energy cost related to the long wavelength mode than that of classical spherical phases.

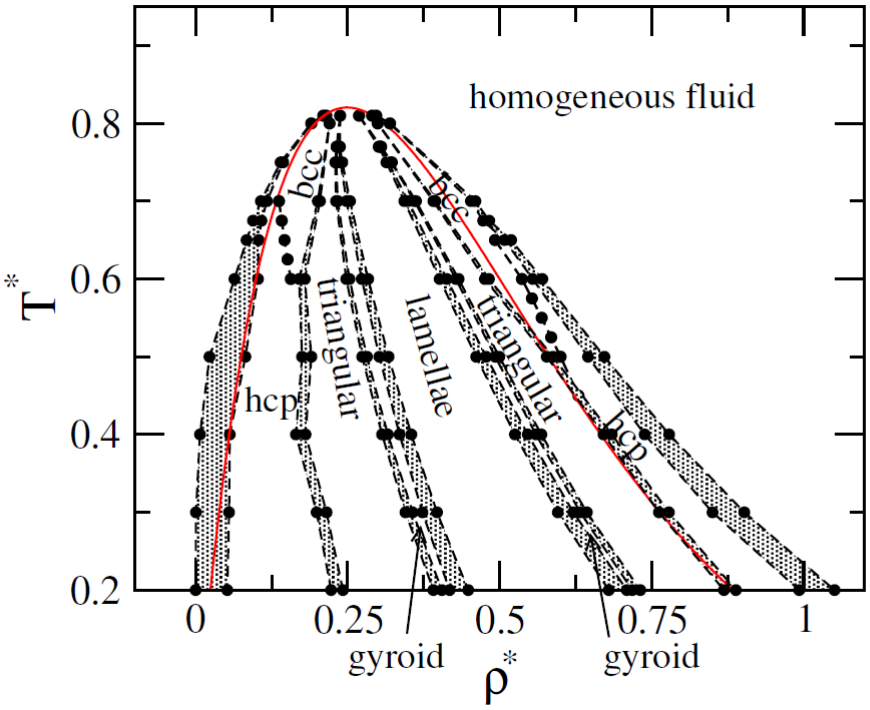

FIGURE 1.5: Phase diagram calculated by D.Pini and A.Parola for hard-sphere fluid with SALR interaction potential. The authors used local density approximation cDFT theory and found HCP, BCC and gyroid phases are stable. This phase diagram is reprinted from reference [38].

Sooner after, Xie *et al.* studied the phase behaviour of interacting hard spheres with inter-particle interaction potentials specially designed to favor the formation of the Frank-Kasper phases [14]. Their results revealed that the Frank-Kasper phases (A15 and σ) could be stable in hard-sphere systems with appropriate SALR interactions. The details of their studies will be presented in later sections. These previous studies have relied on density functional theory with local density approximation, which approximates the excess free energy of hard cores via the equation of state for homogeneous hard-sphere fluids, namely, the Carnahan-Starling equation

[12]. In this thesis, we provide further evidence to the universality of the emergence of the Frank-Kasper phases in interacting hard spheres by applying classical density functional theories based on the lattice gas model and the fundamental measure theory (FMT).

1.3 The organization of this thesis

We have seen that Frank-Kasper phases emerge in various soft matter systems. Here, we focus on the emergence of Frank-Kasper phases in colloidal systems, which are modelled as hard sphere. In Chapter 2, three hard-sphere models – lattice gas model, local density approximation, and fundamental measure theories – are introduced. In Chapter 3, we present our main results: the phase diagrams for different models and inter-particle potentials. We also discuss the differences and similarities of the results obtained from the three models. In Chapter 4, we provide a summary of our main results and suggest some improvements that can be made in future work.

Chapter 2

Theory and Method

2.1 Introduction

The density functional theory was first invented by Hohenberg and Kohn in 1964 to study the ground state of inhomogeneous electron gas in an external potential $V(r)$. They proved a simple yet powerful theorem: at zero temperature, the external potential is a unique functional of the one-body density distribution of the system. Later in 1964, Mermin pointed out that this theorem can be extended to finite temperature system, and now it is known as the Hohenberg-Kohn-Mermin (HKM) theorem. Although the HKM theorem was originally discovered in quantum systems, it is also applicable to classical systems. The classical density functional theory, which closely follows the quantum density functional theory, was established in the 1970s. The classical density functional theory quickly became an important tool in the theory of liquids. In 1976, Percus studied the density functional theory for one-dimensional hard rods [36]. He presented the exact free energy functional form of 1D hard rods and also gave a hint on approximating the free energy functional form of higher-dimensional cases, i.e., 2D hard disks and

3D hard spheres. Later in the 1980s, inspired by Percus's idea, Rosenfeld developed the fundamental measure theory (FMT) for 3D hard spheres based on the weighted density approximation (WDA) [43]. Rosenfeld's FMT was the most successful theory in terms of describing the properties of hard-sphere fluids in different situations, i.e., fluids adsorbed at the wall and confined fluids [11]. However, the FMT completely failed in describing solid structures due to the divergence issue that appears in the excess free energy. After that, Tarazona and Rosenfeld modified the divergent part in the free energy functional and fixed this issue empirically [42]. Later on, they solved the problem systematically by introducing a rank-two weighted density tensor [52]. Nowadays, the classical density functional theory has become a powerful and versatile tool to study the structure and thermodynamic quantities of fluids and crystals.

2.2 Classical density functional theory

All version of the density functional theories are based on the HKM theorem [59]: The external potential $V_{ext}(\vec{r})$ alone gives rise to a unique density distribution $\rho(\vec{r})$ regardless of the inter-particle interaction. In other words, the external potential and one-body density distribution are in one-to-one correspondence, despite the external potential being usually zero in most cases. For a specific system, if the temperature T, chemical potential μ, and inter-particle interaction potential $V(r)$ are specified, the Helmholtz free energy $F[\rho(\vec{r})]$ is a unique functional of the one-body density distribution function $\rho(r)$, and this functional form is independent of the external potential. The true equilibrium density profile $\rho_{eq}(\vec{r})$ minimizes the free energy functional and gives the grand potential. Therefore, once the correct

free energy functional is defined, we can obtain the equilibrium density profile via the variational method. In the grand canonical ensemble, the free energy functional is given by,

$$\Omega[\rho(\vec{r})] = F[\rho(\vec{r})] + \int d\vec{r}\rho(\vec{r})(V_{ext}(\vec{r}) - \mu). \tag{2.1}$$

The equilibrium density distribution is obtained by minimizing the grand potential:

$$\frac{\delta\Omega[\rho(\vec{r})]}{\delta\rho(\vec{r})} = \frac{\delta F[\rho(\vec{r})]}{\delta\rho(\vec{r})} + V_{ext}(\vec{r}) - \mu = 0. \tag{2.2}$$

The $V_{ext}(\vec{r})$ is normally set to be zero. And for a hard-sphere system, the Helmholtz free energy is split into three parts: the contribution from ideal gas $F_{id}[\rho]$, the excess part due to the volume excluded effect $F_{ex}^{HS}[\rho]$ and the part contributed by non-local pairwise interaction $\omega(\vec{r})$:

$$F[\rho] = F_{id}[\rho] + F_{ex}^{HS}[\rho] + F_{ex}^{MF}[\rho]. \tag{2.3}$$

The ideal gas part F_{id} is simple and has an exact form. However, the form of excess part F_{ex}^{HS} depends on the specific approximation to the hard-sphere excluded volume effect. The last term F_{ex}^{MF} represents the non-local pairwise interaction and is treated approximately. It is usually written in terms of the Fourier transformation to reduce the convolution to simple multiplication:

$$F_{ex}^{MF}[\rho] = \frac{1}{2}\int d\vec{r'}\int d\vec{r}\rho(\vec{r})\rho(\vec{r'})\omega(\vec{r}-\vec{r'}) = \frac{1}{2}\sum_{\vec{k}}|\rho(\vec{k})|^2\omega(\vec{k}). \tag{2.4}$$

2.3 The Density Functional Theory of an Ideal Gas

The grand partition function of an ideal gas subject to a external potential $V_{ex}(\vec{r})$ can be expressed as [55]:

$$Z_{id} = \sum_{N=0}^{\infty} \frac{e^{\beta\mu N}}{N!\Lambda^{3N}} \left(\int d\vec{r} e^{-\beta V_{ext}(\vec{r})} \right)^N, \tag{2.5}$$

where Λ is the thermal wavelength $h/\sqrt{2\pi m k_B T}$ and is usually set to be 1. The above equation can be simplified via the mathematical relation: $e^x = \sum_{m=0}^{\infty} x^m/m!$, which gives,

$$Z_{id} = \exp\left[\frac{e^{\beta\mu}(\int d\vec{r} e^{-\beta V_{ext}(\vec{r})})}{\Lambda^3} \right]. \tag{2.6}$$

One can find the grand potential of the ideal gas from its partition function:

$$\beta\Omega_{id} = -\ln(Z_{id}) = -\frac{1}{\Lambda^3} e^{\beta\mu} \int d\vec{r} e^{-\beta V_{ext}(\vec{r})}. \tag{2.7}$$

Then the first order variation of grand potential with respect to $V_{ext}(\vec{r})$ gives the one-body density distribution:

$$\rho(\vec{r}) = \frac{\delta\Omega_{id}}{\delta V_{ext}} = \frac{1}{\Lambda^3} e^{\beta\mu} e^{-\beta V_{ext}(\vec{r})}. \tag{2.8}$$

Therefore, the grand potential and external potential are expressed in terms of $\rho(\vec{r})$:

$$\beta\Omega_{id} = -\int d\vec{r} \rho(\vec{r}). \tag{2.9}$$

leading to,

$$\beta V(\vec{r})_{ext} = -\ln(\Lambda^3 \rho(\vec{r})) + \beta\mu. \tag{2.10}$$

Substituting them back to equation (2.1), one can find the exact Helmholtz free energy expression for an ideal gas:

$$\beta F_{id}[\rho] = \int d\vec{r}\rho(\vec{r}) \left[\ln(\rho(\vec{r})\Lambda^3) - 1\right]. \tag{2.11}$$

In contrast to the exact ideal gas free energy, the excess free energy, including the entropy reduction due to the hard-sphere excluded effect, does not have an exact expression. One goal of classical density functional theory is to find a better approximation for the excess free energy part. In the past few decades, several versions of hard-sphere model to approximate the excess free energy, such as lattice gas model, Caranhan-Starling approximation and fundamental measure theory have been developed. All three theories will be introduced in this chapter.

2.4 Inter-particle interaction potential

In this study, in addition to the hard-core interaction, we consider an inter-particle potential that is pairwise additive, and spherically symmetric. The potential consists of two Gaussian functions with opposite signs, resulting in a short-range attractive and long-range repulsive (SALR) potential profile. The generic form is given by,

$$U(r) = \epsilon\Big\{ - A\exp[\frac{-(r-d_1)^2}{\sigma_1^2}] + \exp[-\frac{(r-d_2)^2}{\sigma_2^2}]\Big\}. \tag{2.12}$$

The parameters are defined in the following way: ϵ is the unit of energy, A is the relative strength between two Gaussian functions. d_1 and d_2 are the centers of the

Gaussian functions in unit of diameter of hard-sphere σ. σ_1 and σ_2 are the width of the Gaussian functions in the unit of σ as well. To determine these parameters, we follow the convention in [13] by requiring that the integral of potential over space is zero, i.e.:

$$\int d\vec{r}U(\vec{r}) = \iint 4\pi r^2 \sin(\theta)U(r)drd\theta = 0. \tag{2.13}$$

This is equivalent to set the Fourier transform of $U(r)$ at $k = 0$ is zero: $\lim_{k\to 0}\omega(k) = 0$. In this case, we can eliminate A and expressed it in terms of the rest of parameters. The Fourier transform of a spherically symmetric potential is obtained via:

$$\begin{aligned} w(k) =& \int d\vec{r}U(|\vec{r}|)e^{-i\vec{k}\cdot\vec{r}} \\ =& \int_0^{\infty}\int_0^{\pi}\int_0^{2\pi} r^2\sin\theta drd\theta d\phi U(r)e^{-ikr\cos\theta} \\ =& \int_0^{2\pi} d\phi \int_0^{\infty}\left[\int_0^{\pi} e^{-ikr\cos\theta}\sin\theta d\theta\right] r^2U(r)dr \\ =& \frac{4\pi}{k}\int_0^{\infty}\sin(kr)rU(r)dr. \end{aligned} \tag{2.14}$$

The Gaussian functions' centers are not situated at the origin, thus the Fourier transform of the potential consist of complex error functions that is a highly intricate expression. Owing to its complexity, the explicit expression is not provided here; however, an analytical expression exists and can be computed using mathematical software, such as Mathematica or MATLAB. Here we list two set of

parameters used in our calculaton:

$$\begin{cases} \text{set } 1: A = 1.9993, d_1 = 1, d_2 = 2, \sigma_1 = 1, \sigma_2 = 1 \\ \text{set } 2: A = 0.7617, d_1 = 1.5, d_2 = 2.3, \sigma_1 = 0.5, \sigma_2 = 1.2 \end{cases} \tag{2.15}$$

The potentials produced by these two sets of parameter are called generic double Gaussian 1 (GDG1) and generic double Gaussian 2 (GDG2), respectively. In the figures below, we present the two potentials both in the real space and the Fourier space. As shown in Figure 2.1 (a), the potential $\mathrm{GDG}_1(r)$ exhibits the typical SALR shape, while the potential $\mathrm{GDG}_2(r)$ features a minor attractive well subsequent to the repulsive bump. It is important to note that the k value corresponding to the global minimum of $\omega(k)$ is related to the distance (L_0) between the nearest neighbor clusters. We can estimate the period of lamellar phase via the relation: $\frac{2\pi}{k_{\text{mini}}} = L_0$ [37]. Periods of other phases can be estimated by geometric relation, e.g. $L_{\text{BCC}} = \sqrt{2}L_0$.

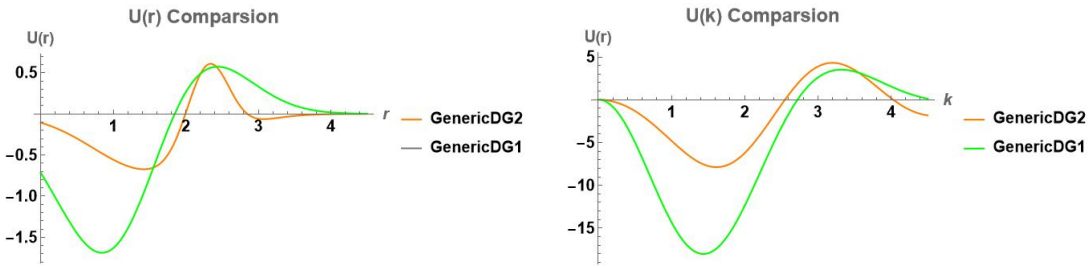

(A) (B)

FIGURE 2.1: The potentials in the real space and the Fourier space are plotted in (a) and (b) respectively.

2.5 Lattice Gas Model

The fundamental concept of the lattice gas model is straightforward: All particles are situated on lattice sites, and the hard-core excluded volume effect is incorporated by allowing each lattice site to be either empty or occupied by a single particle. The lattice gas model solely accounts for translational entropy, making it quantitatively accurate when the temperature is low and the cluster size is significantly larger than the lattice constant [49]. We start the derivation from defining the Hamiltonian of lattice gas model:

$$H = \frac{1}{2}\sum_{ij} n_i V_{ij} n_j - \mu \sum_i n_i, \tag{2.16}$$

where n_i label the occupied sites and V_{ij} is the interaction potential between two sites. The summation counts all the pairs of lattice sites. One can find the grand partition function:

$$Z = \sum_{n_i} e^{-\beta H\{n_i\}} = \sum_{n_i} \exp\left[-\frac{\beta}{2}\sum_{ij} n_i V_{ij} n_j + \beta\mu \sum_i n_i\right]. \tag{2.17}$$

In order to transform the particle theory to a field theory, we apply the standard Hubbard-Stratonovich transformation to the partition function:

$$\exp\left[-\frac{1}{2}\sum_{ij} n_i V_{ij} n_j\right] = \frac{1}{N}\int D\phi \exp\left[-\frac{1}{2}\sum_{ij}\phi_i V_{ij}^{-1}\phi_j + i\sum_j \phi_j n_j\right]. \tag{2.18}$$

Also, the value of n_i can only be 1 or 0. Hence, we get,

$$Z = \frac{1}{N}\int D\phi \exp\left[-\frac{1}{2\beta}\sum_{ij}\phi_i V_{ij}^{-1}\phi_j + \sum_j \ln(1+\exp[i\phi_j + \beta\mu])\right]. \tag{2.19}$$

The partition function is expressed as a functional integral. Then we can apply the saddle-point approximation and ignore the normalization constant:

$$Z = \exp\left\{ -\frac{1}{2\beta}\sum_{ij}\phi_i V_{ij}^{-1}\phi_j + \sum_j \ln(1+\exp[i\phi_j+\beta\mu])\right\}. \tag{2.20}$$

The grand potential density per unit volume is written as,

$$\beta\Omega = -\frac{\ln(Z)}{V} = -\frac{1}{2\beta V}\sum_{ij}\phi_i V_{ij}^{-1}\phi_j + \frac{1}{V}\sum_j \ln\left(1+\exp[i\phi_j+\beta\mu]\right). \tag{2.21}$$

The summation can be converted to integral by taking the continuum limit:

$$\sum_j = \frac{1}{a^d}\int dx^d, \tag{2.22}$$

where a is the lattice constant and d is the dimension. We can define the maximum packing density as $\rho_m = \frac{1}{a^3}$:

$$\beta\Omega = \frac{1}{2\beta\rho_m V}\int d\vec{r}\int d\vec{r'}\phi(\vec{r})V^{-1}(\vec{r}-\vec{r'})\phi(\vec{r'}) - \frac{1}{\rho_m V}\int d\vec{r}\ln(1+\exp(i\phi(\vec{r})+\beta\mu)). \tag{2.23}$$

In the above equation, the term $i\phi(\vec{r})+\beta\mu$ behave likes an external field. Therefore, we can use the same method in equation (2.8) to find the density distribution:

$$\rho(\vec{r}) = \frac{\delta(\beta\Omega)}{\delta(i\phi(\vec{r})+\beta\mu)} = \rho_m\frac{e^{i\phi(\vec{r})+\beta\mu}}{1+i\phi(\vec{r})+\beta\mu}. \tag{2.24}$$

Also we can minimize the grand potential with respect $\phi(\vec{r})$ and use equation (2.24) to eliminate $1 + \exp(i\phi(\vec{r}) + \beta\mu)$:

$$\frac{\rho_m^2}{\beta V}\int d\vec{r'}V^{-1}(\vec{r}-\vec{r'})\phi(\vec{r'}) - \frac{i\rho(\vec{r})}{V} = 0. \tag{2.25}$$

Applying the Fourier transform, we get,

$$\phi(\vec{k}) = \frac{i\beta\rho(\vec{k})V(\vec{k})}{\rho_m^2}. \tag{2.26}$$

From equation (2.26), we can find $\phi(\vec{r})$ is purely imaginary and hence $i\phi(\vec{r})$ can be replaced by $-\phi(\vec{r})$ for convenience. And hence equation (2.24) and (2.26) become:

$$\rho(\vec{r}) = \rho_m \frac{e^{-\phi(\vec{r})+\beta\mu}}{1+e^{-\phi(\vec{r})+\beta\mu}}, \tag{2.27}$$

$$\phi(\vec{k}) = \frac{\beta\rho(\vec{k})V(k)}{\rho_m^2}. \tag{2.28}$$

In real space, equation (2.28) is rewritten as,

$$\phi(\vec{r}) = \frac{\beta}{\rho_m^2}\int d\vec{r}V(\vec{r}-\vec{r'})\rho(\vec{r'}). \tag{2.29}$$

In order to get rid of $\phi(\vec{r})$ and $V^{-1}(\vec{r}-\vec{r'})$ in the grand potential equation (2.23), we substitute equation (2.24) and (2.29) into it, which leads to,

$$\begin{aligned}\beta\Omega &= \frac{\beta^2}{2\rho_m^2 V}\int d\vec{r}\int d\vec{r'}\int d\vec{r_1}\int d\vec{r_2}\rho(\vec{r_1})V(\vec{r}-\vec{r_1})V^{-1}(\vec{r}-\vec{r'})\rho(\vec{r_2})V(\vec{r'}-\vec{r_2}) \\ &\qquad + \frac{\rho_m}{V}\int d\vec{r}\ln(1-\frac{\rho(\vec{r})}{\rho_m}) \\ &= \frac{\beta^2}{2\rho_m^2 V}\int d\vec{r'}\int d\vec{r_1}\int d\vec{r_2}\rho(\vec{r_1})\Big\{\int d\vec{r}V(\vec{r}-\vec{r_1})V^{-1}(\vec{r}-\vec{r'})\Big\}\rho(\vec{r_2})V(\vec{r'}-\vec{r_2}) \\ &\qquad + \frac{\rho_m}{V}\int d\vec{r}\ln(1-\frac{\rho(\vec{r})}{\rho_m}) \\ &= \frac{\beta^2}{2\rho_m^2 V}\int d\vec{r'}\int d\vec{r_1}\int d\vec{r_2}\rho(\vec{r_1})\delta(\vec{r_1}-\vec{r'})\rho(\vec{r_2})V(\vec{r'}-\vec{r_2}) + \frac{\rho_m}{V}\int d\vec{r}\ln(1-\frac{\rho(\vec{r})}{\rho_m}) \\ &= \frac{\beta^2}{2\rho_m^2 V}\int d\vec{r_1}\int d\vec{r_2}\rho(\vec{r_1})\rho(\vec{r_2})V(\vec{r_1}-\vec{r_2}) + \frac{\rho_m}{V}\int d\vec{r}\ln(1-\frac{\rho(\vec{r})}{\rho_m}). \quad (2.30)\end{aligned}$$

In equation (2.30), the chemical potential μ is cancelled. We need to put it back in order to construct the phase diagram. The first step is to split the last term in equation (2.30):

$$\begin{aligned}\frac{\rho_m}{V}\int d\vec{r}\ln(1-\frac{\rho(\vec{r})}{\rho_m}) = \frac{1}{V}\int d\vec{r}\Big\{&\rho(\vec{r})\ln(1-\frac{\rho(\vec{r})}{\rho_m}) \\ &+ [\rho_m - \rho(\vec{r})\ln(1-\frac{\rho(\vec{r})}{\rho_m})]\Big\}. \quad (2.31)\end{aligned}$$

Also, from equation (2.24) we get

$$\rho_m - \rho(\vec{r}) = \frac{\rho(\vec{r})}{e^{-\phi(\vec{r})+\beta\mu}}. \quad (2.32)$$

We can insert it into equation (2.30). Then we combine the result with equation (2.31) and get a simplified expression:

$$\begin{aligned}\beta\Omega = \frac{\beta^2}{2\rho_m^2 V}\int d\vec{r_1}\int d\vec{r_2}\rho(\vec{r_1})\rho(\vec{r_2})V(\vec{r_1}-\vec{r_2}) \\ + \frac{1}{V}\int d\vec{r}\Big\{\rho(\vec{r})\ln(\frac{\rho(\vec{r})}{\rho_m}) + [\rho_m - \rho(\vec{r})\ln(1-\frac{\rho(\vec{r})}{\rho_m})]\Big\} \\ + \frac{1}{V}\int d\vec{r}\rho(\vec{r})[\phi(\vec{r})-\beta\mu]. \quad (2.33)\end{aligned}$$

Finally, we use the Legendre transformation to eliminate $\phi(\vec{r})$ and get the proper grand potential for phase diagram construction:

$$\begin{aligned}\beta\tilde{\Omega} &= \beta\Omega - \frac{1}{V}\int d\vec{r}\phi(\vec{r})\rho(\vec{r}) \\ &= \frac{\beta}{2\rho_m^2 V}\int d\vec{r_1}\int d\vec{r_2}\rho(\vec{r_1})\rho(\vec{r_2})V(\vec{r_1}-\vec{r_2}) \\ &+ \frac{1}{V}\int d\vec{r}\Big\{\rho(\vec{r})\ln(\frac{\rho(\vec{r})}{\rho_m}) + [\rho_m - \rho(\vec{r})\ln(1-\frac{\rho(\vec{r})}{\rho_m})]\Big\} - \frac{\beta\mu}{V}\int d\vec{r}\rho(\vec{r}).\end{aligned} \quad (2.34)$$

Equation (2.34) is the grand potential expression that we used to construct the phase diagram. The iterative equation for density distribution can be obtained by minimizing equation (2.34) with respect to $\rho(\vec{r})$:

$$\frac{\delta(\beta\tilde{\Omega})}{\delta\rho(\vec{r})} = \frac{\beta}{\rho_m^2 V}\int d\vec{r'}V(\vec{r}-\vec{r'})\rho(\vec{r}) + \frac{1}{V}\ln(\frac{\rho(\vec{r})}{\rho_m-\rho(\vec{r})}) - \frac{\beta\mu}{V} = 0. \quad (2.35)$$

Using the convolution property of the Fourier transform, we can find the self-consistent equation for $\rho(\vec{r})$:

$$\rho(\vec{r}) = \frac{e^{\mu - \frac{1}{\rho_m^2}\mathcal{F}^{-1}[V(\vec{k})\rho(\vec{k})]}}{1 + e^{\mu - \frac{1}{\rho_m^2}\mathcal{F}^{-1}[V(\vec{k})\rho(\vec{k})]}}, \tag{2.36}$$

where $\mathcal{F}^{-1}$ donates the inverse Fourier transform. And β is absorbed into $V(\vec{k}|)$, i.e. $V(\vec{k}) = \beta\mathcal{F}[V(\vec{r})]$. The goal is to find the solution of equation (2.36), and the numerical minimization details are presented later in this chapter. The above derivation assumes V_{ij} is invertible. However, if V_{ij} oscillates around zero, it has zeros that not invertible. We need to decompose the potential into two positive pieces: $V_{ij} = V_+ - V_-$, and then apply the Hubbard-Stratonovich transformation. An analysis of non-invertible case can be found in reference [49]. The final expressions for the grand potential and density distribution function remain the same.

2.6 Local density approximation method

The local density approximation (LDA) is a commonly used assumption if the density profile does not change abruptly. In other words, the inhomogenous fluid is under the slow-modulation limit [11]:

$$\frac{|\nabla\rho(\vec{r})|}{\rho_0} \ll \frac{1}{\xi_0}, \tag{2.37}$$

where ξ_0 is the typical correlation length of the fluid and ρ_0 is bulk density. In this case, the excess free energy functional form is a functional of $\rho(\vec{r})$, and does not depend on higher order gradient of $\rho(\vec{r})$, i.e. $\nabla\rho(\vec{r})$. Therefore the local excess

free energy density can be written as,

$$\Phi_{LDA} = \Phi[\rho(\vec{r})]. \tag{2.38}$$

The expression of $\Phi([\rho(\vec{r})])$ can be obtained from the equation of state of homogeneous hard-sphere fluid, such as Percus-Yevick (PY) equation and Caranhan-Starling (CS) equation [5, 35]. Then the total excess free energy is given by,

$$\Phi_{total}(\rho(\vec{r})) = \int d\vec{r}\Phi_{LDA}[\rho(\vec{r})]. \tag{2.39}$$

The local density approximation for hard-sphere systems is sufficiently accurate when the density varies smoothly across space, or when the particle size is significantly smaller than the cluster size for SALR fluids [38]. In the following, we will demonstrate how to derive the Carnahan-Starling equation of state from the virial expansion. The virial expansion serves as a fundamental basis in the theory of simple liquids. It relates the pressure P, density ρ and temperature T in a series expansion by [60]:

$$\frac{\beta P}{\rho} = 1 + \sum_{n=1}^{\infty} B_n \eta^n, \tag{2.40}$$

where $\eta = \frac{\pi\rho d^3}{6}$ and d is the diameter of hard sphere. B_n is the virial coefficient which can be calculated from an expression involving the inter-particle potential:

$$B_n = \frac{1-n}{n!} \int .... \int V_n \prod_{j=1}^{n} d\vec{r_j}. \tag{2.41}$$

The first few coefficients can by evaluated numerically; however, the integrals become increasingly complex for subsequent terms. You *et al.* calculated the first

eight terms of virial expansion for hard-sphere and expressed it in terms of packing density η [60, 11] :

$$\frac{\beta P}{\rho} = 1 + 4\eta + 10\eta^2 + 18.365\eta^3 + 22.225\eta^4 + 39.74\eta^5 + 53.5\eta^6 + 70.8\eta^7. \quad (2.42)$$

Caranhan and Starling were guided by this expression and constructed a simple yet quite accurate equation of state for homogeneous hard-sphere fluid. By observing the first few coefficients, they rounded the numbers to the nearest integers, i.e. $18.365 \rightarrow 18$, $22.225 \rightarrow 22$. They concluded the integer virial coefficients can be expressed as [5] :

$$B_n = n^2 + n - 2. \quad (2.43)$$

Therefore equation (2.40) becomes,

$$\frac{\beta P}{\rho} = 1 + \sum_{n=2}^{\infty}(n^2 + n - 2)\eta^{n-1} = 1 + \sum_{n=0}^{\infty}(n^2 + 3n)\eta^n. \quad (2.44)$$

Equation (2.44) can be evaluated analytically via geometric series tricks:

$$\sum_{n}^{\infty} nx^n = x\frac{d}{dx}\sum_{n=1}^{\infty} x^{n-1} = \frac{x}{(x-1)^2}, \quad (2.45)$$

and

$$\sum_{n}^{\infty} n^2x^n = x^2\frac{d^2}{dx^2}\sum_{n=1}^{\infty} x^{n-2} + \sum_{n=1}^{\infty} nx^n = \frac{x(1+x)}{(1-x)^3}, \quad (2.46)$$

which leads to the Caranhan-Starling equation of state for homogeneous hard-sphere fluid [5] :

$$\frac{\beta P}{\rho} = \frac{1 + \eta + \eta^2 - \eta^3}{(1-\eta)^3}. \quad (2.47)$$

The Caranhan-Starling equation of state can be used conveniently to approximate the excess free energy of hard-sphere fluid in density functional theory. Using the thermodynamic relations:

$$P = (\frac{\partial F}{\partial V})_{T,N} = \frac{\partial F}{N\partial(\frac{1}{\rho})}, \tag{2.48}$$

one can obtain an expression for the excess free energy in terms of packing density η [11] :

$$\frac{\beta F^{ex}}{N} = \int_0^{\eta'} (\frac{\beta P}{\rho} - 1)\frac{d\eta'}{\eta'} = \frac{\eta(4-3\eta)}{(1-\eta^2)}. \tag{2.49}$$

Therefore, we can find the grand potential of Caranhan-Starling approximation by adding the ideal gas contribution and non-local inter-particle interaction:

$$\beta\Omega = \frac{1}{V}\int d\vec{r}\rho(\vec{r})\Big\{\ln(\rho(\vec{r})-\mu-1+\frac{\eta(4-3\eta)}{(1-\eta^2)}\Big\}+\mathcal{F}^{-1}\{\frac{1}{2V}\sum_{\vec{k}}|\rho(\vec{k})|^2\omega(\vec{k})\}. \tag{2.50}$$

The equilibrium density profile is obtained by minimizing the grand potential:

$$\frac{\delta(\beta\Omega)}{\delta\rho(\vec{r})} = \frac{1}{V}\left[\ln\rho(\vec{r}) - \mu + \frac{\eta(8-9\eta+3\eta^2)}{(1-\eta)^3}\right] + \frac{1}{V}\mathcal{F}^{-1}\Big\{\rho(\vec{k})w(k)\Big\} = 0. \tag{2.51}$$

The density functional theory combined with the Carnahan-Starling approximation has been used to study cluster phases formed by hard-sphere fluid with SALR inter-particle interaction [38, 37]. However, as mentioned earlier, the LDA method is a suitable approximation only if the slow-modulation limit is satisfied. If we would like to explore the internal structure of clusters or if the size of a cluster is comparable to the size of a hard sphere, new approximation methods that go

beyond the LDA, such as Rosenfeld's fundamental measure theory are required. Instead of using the local-density approximation, Rosenfeld's FMT treats the excess free energy as a functional of a set of weighted densities $n_\alpha[\rho]$, i.e., $\Phi_{\mathrm{WDA}}\{n_\alpha[\rho]\}$.

2.7 Fundamental measure theory

2.7.1 Rosenfeld's fundamental measure theory

The motivation for Rosenfeld's FMT comes from Percus's DFT for one-dimensional hard rods. In the 1-D hard rod model, the rods can only interact with their nearest neighbors, as they cannot pass over each other. The 1-D hard rods may seem like an oversimplified model, but it has an exact expression for the excess free energy and provides some insights for higher-dimensional cases. The Helmholtz free energy of 1D hard rod without pairwise inter-particle interaction is given by [36]:

$$\beta F[\rho(x)] = \beta F_{\mathrm{id}}[\rho(x)] - \frac{1}{2}\int \left[\rho(x+\frac{d}{2}) + \rho(x-\frac{d}{2})\right] \ln\left(1 - \int_{-\frac{d}{2}}^{\frac{d}{2}} (\rho(x+y)dy)\right) dx, \tag{2.52}$$

where d is the diameter of hard rod. The excess free energy depends on two quantities: the density integral over the surface of rod ($\rho(x \pm d/2)$) which is centered at x; and the density integral over the volume of hard rod ($\rho(x+y)$) [24]. Therefore, the above expression can be expressed in terms of weighted densities which are defined as follows:

$$\beta F_{\mathrm{ex}}[n_\alpha] = -\int_{-\infty}^{\infty} n_s(\rho(\vec{r})) \ln\left[1 - n_v \rho(\vec{r})\right] d\vec{r}, \tag{2.53}$$

where n_α is weighted densities, n_s and n_v label the density integral over the surface and the volume respectively:

$$n_s(\rho) = \int_{-\infty}^{\infty} w_s(r-y)\rho(y)dy, \tag{2.54}$$

$$n_v(\rho) = \int_{-\infty}^{\infty} w_v(r-y)\rho(y)dy, \tag{2.55}$$

where w_α are the weight functions which restrict the integrals on hard rod's surface and volume. They are defined as:

$$w_s = \delta(\frac{d}{2} - |x|), \tag{2.56}$$

$$w_v = \Theta(\frac{d}{2} - |x|), \tag{2.57}$$

where Θ is the Heaviside step function and δ is the Dirac-delta function. Rosenfeld generalized this idea to higher dimensions. He started from the expression of Helmholtz free energy for the low one-body density limit $\rho_i(\vec{r}) \to 0$ [44]:

$$\beta F_{\text{ex}}[\{\rho_i\}] = -\frac{1}{2}\sum_{i,j}\int d\vec{r_1}\int d\vec{r_2}\rho_i(\vec{r_1})f_{ij}(\vec{r_1}-\vec{r_2})\rho(\vec{r_2}), \tag{2.58}$$

where i labels the species of particles and f_{ij} is the Mayer-f function:

$$f_{ij} = \exp\left[-\beta V_{ij}(\vec{r_1}-\vec{r_2})\right] - 1, \tag{2.59}$$

where V_{ij} is pair interaction between two types of particle i and j. In the case of hard-sphere interaction, it is given by,

$$V_{ij} = \begin{cases} \infty & r_{ij} < R_i + R_j, \\ 0 & r_{ij} \geqslant R_i + R_j. \end{cases} \tag{2.60}$$

And the corresponded Mayer-f function is reduced to step function,

$$f_{ij} = \begin{cases} -1 & r_{ij} < R_i + R_j, \\ 0 & r_{ij} \geqslant R_i + R_j. \end{cases} \tag{2.61}$$

Rosenfeld further noticed that the step function can be decomposed as combinations of a set of weighted functions which include four scalar functions and two vector functions:

$$-f_{ij}(r) = \omega_3^i \otimes \omega_0^j + \omega_0^i \otimes \omega_3^j + \omega_2^i \otimes \omega_1^j + \omega_1^i \otimes \vec{\omega}_2^j - \vec{\omega}_2^i \otimes \vec{\omega}_1^j - \vec{\omega}_1^i \otimes \vec{\omega}_2^j. \tag{2.62}$$

The symbol $\otimes$ represents the 3D convolution integral:

$$\omega_i \otimes \omega_j(\vec{r} = \vec{r}_i - \vec{r}_j) = \int d\vec{r'} \omega_i(\vec{r'} - \vec{r}_i)\omega_j(\vec{r'} - \vec{r}_j). \tag{2.63}$$

The weight functions are given by,

$$\omega_3^i(r) = \Theta(R_i - r), \tag{2.64}$$

$$\omega_2^i(r) = \delta(R_i - r), \tag{2.65}$$

$$\omega_1^i(r) = \frac{\omega_2^i(r)}{4\pi R_i}, \tag{2.66}$$

$$\omega_0^i(r) = \frac{\omega_2^i(r)}{4\pi R_i^2}, \tag{2.67}$$

$$\vec{\omega}_2^i(r) = \frac{r}{r}\delta\left(R_i - r\right), \tag{2.68}$$

$$\vec{\omega}_1^i(r) = \frac{\vec{\omega}_2^i(r)}{4\pi R_i}. \tag{2.69}$$

However, this decomposition is not unique; Kierlik and Rosinberg proposed another set of weight functions [15]. Instead of using two vector weight functions, four weight functions containing the first and second derivatives of the Dirac delta function can be used as well. For Rosenfeld's decomposition, if we integrate the four scalar weight functions over space, we obtain the geometric measures of a sphere. For example, the integration of w_3, w_2, w_1, and w_0 yields the volume $4\pi R_i^3/3$, surface area $4\pi R_i^2$, radius R_i, and unity 1, respectively. This is why Rosenfeld named it the fundamental measure theory. Based on these weight functions, a set of weighted densities is defined as follows:

$$n_\alpha = \sum_{i=1}^{\nu} \int dr^3 \rho_i(r - r')\omega_\alpha^i(r'). \tag{2.70}$$

Each n_α sums weighted densities of all species ν. In the bulk case, the density profiles: ρ_i, are constant, the vector-like weighted densities vanish and the scalar weighted densities have simple expressions: $n_3 = 4\pi \sum_i \rho_i R_i^3/4$, $n_2 = 4\pi \sum_i \rho_i R_i^2$,

$n_1 = 4\pi \sum_i \rho_i R_i^2$, $n_0 = \sum_i \rho_i R_i$. Those are the scaled-particle variables which play a key role in the derivation of Rosenfeld's FMT. Motivated by the form of equation (2.53), Rosenfeld assumed the excess free energy functional can be expressed in terms of weighted densities [44] :

$$\beta F_{\text{ex}} \left[\{\rho_i\}\right] = \int d\vec{r} \Phi \left(\{n_\alpha \left(\vec{r}\right)\}\right). \tag{2.71}$$

The above equation is unitless, and hence $\Phi\{n_\alpha\}$ has the unit of $1/\text{length}^3$. Naturally, Φ can be written as a linear combination of weighted densities. Using dimensional analysis, the possible terms are n_0, $n_1 n_2$, n_2^3, $\vec{n}_1 \cdot \vec{n}_2$ and $\vec{n}_2 \cdot \vec{n}_2$ with dimensionless coefficients $f_i(n_3)$ [11, 24]:

$$\Phi = f_0\left(n_3\right) n_0 + f_1\left(n_3\right) n_1 n_2 + f_2\left(n_3\right)\left(\overrightarrow{n_1}\cdot\overrightarrow{n_2}\right) + f_3\left(n_3\right) n_2^3 + f_4\left(n_3\right) n_2 (\overrightarrow{n_2}\cdot\overrightarrow{n_2}). \tag{2.72}$$

To determine the exact expressions for coefficients f_i, Rosenfeld input the scaled-particle (SPT) equation:

$$\lim_{R->\infty} \frac{\beta \mu^{ex}}{V} = \beta P, \tag{2.73}$$

where $V = 4\pi R_i^3/3$ is the volume of particle. The SPT equation simply relates the excess chemical potential μ^{ex} to the pressure P. The excess chemical potential of inserting a big sphere into homogeneous fluid equal to the work which can create a same size cavity in the system with pressure P. The excess chemical potential can also be expressed in terms of excess grand potential:

$$\frac{\beta \mu_i^{\text{ex}}}{V} = \frac{1}{V}\frac{\partial \Phi}{\partial \rho_i} = \frac{1}{V}\sum_\alpha \frac{\partial \Phi}{\partial n_\alpha}\frac{\partial n_\alpha}{\partial \rho_i}. \tag{2.74}$$

In the case of homogeneous fluid, only the term $\partial n_3/\partial\rho$ is non-vanishing at the limit of $R \to \infty$, which leads to,

$$\lim_{R->\infty} \frac{\beta\mu_{\text{ex}}}{V} = \frac{\partial\Phi}{\partial n_3} = \beta P. \tag{2.75}$$

Another assumption made in FMT is that equation (2.75) holds for inhomogenous fluids. The grand potential density can be expressed as,

$$\Omega_{\text{bulk}} = \Phi + \Omega_{\text{id}} - \sum_i \mu_i \rho_i. \tag{2.76}$$

Now, we combine equation (2.9), (2.75), (2.76) and the thermodynamic relation $\Omega_{\text{bulk}} = -PV$ together, to get a differential equation:

$$\frac{\partial\Phi}{\partial n_3} = -\Phi + \frac{1}{V}\sum_\alpha \frac{\partial\Phi}{\partial n_\alpha} n_\alpha + n_0. \tag{2.77}$$

Substituting equation (2.72) into the above expression, we get a set of differential equations:

$$\frac{df_0(n_3)}{dn_3} = 1 + n_3\frac{df_0(n_3)}{dn_3}, \tag{2.78}$$
$$\frac{df_1(n_3)}{dn_3} = f_1(n_3) + n_3\frac{df_1(n_3)}{dn_3}, \tag{2.79}$$
$$\frac{df_2(n_3)}{dn_3} = 2f_2(n_3) + n_3\frac{df_2(n_3)}{dn_3}, \tag{2.80}$$
$$\frac{df_3(n_3)}{dn_3} = f_3(n_3) + n_3\frac{df_3(n_3)}{dn_3}, \tag{2.81}$$
$$\frac{df_4(n_3)}{dn_3} = 2f_4(n_3) + n_3\frac{df_4(n_3)}{dn_3}. \tag{2.82}$$

These equations can be solved analytically and the integration constants are determined by satisfying free energy and second order variational derivative at the low-density limit [11, 44]. The detailed calculations can be found in reference [6]. The solutions of differential equations are given by [45] :

$$f_0(n_3) = -\ln(1-n_3), \tag{2.83}$$

$$f_1(n_3) = \frac{1}{1-n_3}, \tag{2.84}$$

$$f_2(n_3) = -f_1(n_3), \tag{2.85}$$

$$f_3(n_3) = \frac{1}{24\pi(1-n_3)^2}, \tag{2.86}$$

$$f_4(n_3) = -3f_3(n_3). \tag{2.87}$$

Therefore, the excess free energy density is written in the following form:

$$\Phi = -n_0 \ln(1-n_3) + \frac{n_1 n_2 - \vec{n}_1 \cdot \vec{n}_2}{1-n_3} + \frac{n_2^3 - 3n_2 \vec{n}_2 \cdot \vec{n}_2}{24\pi(1-n_3)^2}. \tag{2.88}$$

In the bulk limit, the FMT excess free energy can be expressed in terms of SPT variables [11]:

$$\Phi = -\xi_0 \ln(1-\xi_3) + \frac{\xi_1 \xi_2}{1-\xi_3} + \frac{\xi_2^3}{24\pi(1-\xi_3)^2}. \tag{2.89}$$

Interestingly, if we use the PY equation of state:

$$\frac{\beta\rho}{P} - 1 = \frac{1+\eta+\eta^2}{(1-\eta)^3}, \tag{2.90}$$

and perform the exact same integral in equation (2.49), we would get the excess free energy from PY equation:

$$\frac{\beta F^{ex}}{N} = -\ln(1-\eta) + \frac{3\eta}{1-\eta} + \frac{3\eta^2}{2(1-\eta)^2}. \tag{2.91}$$

And it is identical to the equation (2.89), if we replace N by ρV and express it in terms of SPT variables. Indeed, we can obtain the same equation of state (2.90) and free energy density (2.91) from scaled-particle theory [11]. This shows the thermodynamic consistency of Rosenfeld's FMT: the theory starts from the SPT equation which only provides the thermodynamic relation. By making a series of reasonable assumptions and using dimensional analysis, we obtain an expression of excess free energy. In the bulk limit, the excess free energy density is reduced to that of PY equation of state (or SPT equation).

2.7.2 Fundamental measure theory white bear version

In principle, the Rosenfeld's FMT can also be derived from the PY equation of state, which implies we can further improve the accuracy of FMT by using a more accurate equation of state. Indeed, Roth *et al.* [45] and Wu *et al.* [61] were able to independently construct a new fundamental measure theory, which is named FMT white bear version (FMT-WB) or modified FMT (MFMT), based on the Marsoori-Carnahan-Starling-Leland equation of state (MCSL) [25]. The MCSL equation is a generalization of Caranhan-Starling equation (2.47), which describes the state of multiple components hard-sphere mixtures:

$$\beta P = \frac{n_0}{1-n_3} + \frac{n_1 n_2}{(1-n_3)^2} + \frac{n_2^3}{12\pi(1-n_3)^3} - \frac{n_3 n_2^3}{36\pi(1-n_3)^3}. \tag{2.92}$$

The FMT-WB preserves Rosenfeld original weight functions and coefficient conditions: equation (2.85), equation (2.87). Hence the new grand potential functional is given by,

$$\Phi = f_0(n_3)n_0 + f_1(n_3)(n_1 n_2) + f_3(n_3)(n_2^3 - 3n_2\vec{n}_2 \cdot \vec{n}_2). \tag{2.93}$$

Using the same approach in Rosenfeld's derivation, we have the differential equation:

$$\beta P = -\Phi + \frac{1}{V}\sum_{\alpha}\frac{\partial \Phi}{\partial n_\alpha}n_\alpha + n_0. \tag{2.94}$$

Similarly, we combine equation (2.92), (2.93), (2.94) together and find the solutions:

$$f_0(n_3) = -\ln(1 - n3), \tag{2.95}$$

$$f_1(n_3) = \frac{1}{1 - n_3}, \tag{2.96}$$

$$f_3(n_3) = \frac{n_3 + (1 - n_3)^2 \ln(1 - n_3)}{36\pi n_3^2 (1 - n_3)^2}. \tag{2.97}$$

Finally, we obtain the excess free energy due to the hard core for FMT-WB:

$$\begin{aligned}\Omega_{\text{ex}}^{\text{HS}} = \int d\vec{r}\Phi[\{n_l(\vec{r})\}] = \int d\vec{r}\Bigg\{ - n_0 \ln(1 - n_3) + \frac{n_1 n_2 - \vec{n}_{V1} \cdot \vec{n}_{V2}}{1 - n_3} \\ + \frac{n_2^3 - 3n_2\vec{n}_{V2} \cdot \vec{n}_{V2}}{36\pi}\left[\frac{\ln(1 - n_3)}{n_3^2} + \frac{1}{n_3(1 - n_3)^2}\right]\Bigg\}.\end{aligned} \tag{2.98}$$

The new FMT-WB is very similar to Rosenfeld's FMT but uses a more accurate equation of state for hard-sphere mixture. Wu *et al.* compared the results obtained by Monte Carlo simulation to the results of MFMT. They demonstrated that MFMT produces more accurate contact density in inhomogeneous case and pair

correlation functions in homogeneous case [61]. Roth *et al.* used FMT-WB to study the hard-sphere absorbed at hard wall, which shown the FMT-WB produced a better results than Rosenfeld's FMT [45]. However, the new FMT still has some problems. Similar to Rosenfeld's FMT, it is unable to predict the solid freezing transition due to the divergence issue. This can be fixed by using the idea of dimensional crossover [42] or tensor-like weighted density [52]. Another problem appears in FMT-WB or MFMT is the thermodynamic inconsistency. The excess chemical potential is obtained by differentiating the excess Helmholtz free energy with respect to density ρ, and in the bulk limit we have:

$$\frac{\beta\mu^{ex}}{V} = \frac{\partial\Phi}{\partial n_3} + \frac{\partial\Phi}{\partial n_2}\frac{4\pi R^2}{V} + \frac{\partial\Phi}{\partial n_1}\frac{R}{V} + \frac{\partial\Phi}{\partial n_0}\frac{1}{V}. \tag{2.99}$$

In the limit of $R \to \infty$, the leading term is $\frac{\partial\Phi}{\partial n_3}$ which is identified as βP in SPT theory. Recall that Rosenfeld's FMT uses SPT equation (2.73), and the result of $\frac{\partial\Phi}{\partial n_3}$ fully recovered the PY compressibility equation (or SPT equation of state) (2.89). However, if we calculate $\frac{\partial\Phi}{\partial n_3}$ for the current version of FMT, we get,

$$\frac{\partial\Phi}{\partial n_3} = \frac{n_0}{1-n_3} + \frac{n_1 n_2}{(1-n_3)} - \frac{n_2^3(2+n_3^2-5n_3)}{36\pi n_3^2(1-n_3)^3} - \frac{n_2^3\ln(1-n_3)}{18\pi n_3^3}, \tag{2.100}$$

which is clearly not the equation (2.92). We assume it is one-component system when we examine the consistency of theory, but it is derived from the equation of state for multi-component. It has been argued that this inconsistency is immaterial in the one-component case since it only slightly differs from Caranhan-Starling equation of state and it is still more accurate than Rosenfeld's FMT [44, 45]. Later on, Roth *et al.* proposed a new FMT for one-component hard-sphere fluid, marked by FMT white bear II [12]. The FMT-WBII used one component

Caranhan-Starling equation as input and it eliminates the inconsistency.

The grand potential density of FMT-WB without external potential is given by,

$$\beta\Omega = \frac{1}{V}\int d\vec{r}\rho(\vec{r})\left[\ln\rho(\vec{r}) - \mu - 1\right] + \frac{1}{V}\int d\vec{r}\left\{-n_0\ln(1-n_3) + \frac{n_1n_2 - \vec{n}_1\cdot\vec{n}_2}{1-n_3} + \frac{n_2^3 - 3n_2\vec{n}_2\cdot\vec{n}_2}{36\pi}\left[\frac{\ln(1-n_3)}{n_3^2} + \frac{1}{n_3(1-n_3)^2}\right]\right\} + \frac{1}{2}\sum_{\vec{k}}\left|\rho(\vec{k})\right|^2 w(k). \quad (2.101)$$

Similar to the previous two hard-sphere models, the equilibrium density is solve numerically via:

$$\begin{aligned}\frac{\delta\beta\Omega}{\delta\rho(\vec{r})} &= \frac{\delta\beta\Omega_{\text{id}}}{\delta\rho(\vec{r})} + \frac{\delta\beta\Omega_{\text{ex}}^{\text{HS}}}{\delta\rho(\vec{r})} + \frac{\delta\beta\Omega_{\text{ex}}^{\text{MF}}}{\delta\rho(\vec{r})} = 0 \\ \rightarrow\rho(\vec{r}) &= \exp\left\{\mu - V\left[\frac{\delta\beta\Omega_{\text{ex}}^{\text{HS}}}{\delta\rho(\vec{r})} + \frac{\delta\beta\Omega_{\text{ex}}^{\text{MF}}}{\delta\rho(\vec{r})}\right]\right\},\end{aligned} \quad (2.102)$$

where $\Omega_{\text{ex}}^{\text{HS}}$ is expressed by equation (2.98) and $\Omega_{\text{ex}}^{\text{MF}}$ is the last term in equation (2.101). Both Rosenfeld's FMT and FMT-WB uses four scalar weighted densities and two vector-like weighted densities to describe the excess free energy. To numerically solve the equation, many of convolution calculations are needed to perform via the fast Fourier transform (FFTs). For one-component hard-sphere fluid, the minimization process at least requires 22 FFTs.

2.8 The homogeneous solution

If the system is homogeneous, $\rho(\vec{r})$ reduces to a constant ρ_0. We can easily find the homogeneous solutions for three models via equation (2.36), (2.51) and (2.102).

The homogeneous solution of lattice gas model is,

$$\rho_0^{\text{LGM}} = \rho_m \frac{e^{-\phi+\beta\mu}}{1+e^{-\phi+\beta\mu}}, \tag{2.103}$$

with

$$\phi = \frac{\beta\rho\omega(k=0)}{\rho_m^2}. \tag{2.104}$$

The homogeneous solution of Caranhan-Starling approximation becomes,

$$\rho_0^{\text{CS}} = \exp\left\{\mu - \frac{\eta(8-9\eta+3\eta^2)}{(1-\eta^3)} - \mathcal{F}^{-1}\{\rho(\vec{k})\omega(\vec{k})\}\right\}. \tag{2.105}$$

For the FMT-WB, the four scalar weighted densities is reduced to the SPT variables and the two vector-like weighted densities vanish in the one-component bulk limit. Recall the FMT-WB is derived from the MCSL equation of state, and the MCSL equation is reduced to Caranhan-Starling equation in the one-component case. Therefore, it is not surprising that the homogeneous solution of the FMT-WB is identical to equation (2.105),

$$\rho_0^{\text{FMT-WB}} = \exp\left\{\mu - \frac{\eta(8-9\eta+3\eta^2)}{(1-\eta^3)} - \mathcal{F}^{-1}\{\rho(\vec{k})\omega(\vec{k})\}\right\}. \tag{2.106}$$

The homogeneous solutions look trivial, but they can be used to test the validity of codes. It is noteworthy that the term $\mathcal{F}^{-1}\{\rho(\vec{k})\omega(\vec{k})\}$ is zero, because ρ is constant and the last term is a integral of $V(\vec{r})$ over the space. The inter-particle $V(\vec{r})$ is designed such that $\int V(\vec{r})d\vec{r}$ vanishes.

2.9 Numerical implementation of DFTs

The grand potential functional $\Omega(\rho)$ needs to be minimized with respect to the density distribution function $\rho(\vec{r})$ through the variational method: $\delta\Omega/\delta\rho = 0$. This process is numerically demanding, especially in the three-dimensional case. In the case of studying crystalline phases, one way to reduce the complexity of the problem is to assume the density distribution is isotropic at each lattice point. A standard method is the Gaussian density ansatz. The density distribution at each lattice point is Gaussian and the total density profile is given by,

$$\rho(\vec{r}) = n_c(\frac{\alpha}{\pi})^{3/2}\sum_{\vec{R}_i} e^{-\alpha(\vec{r}-\vec{R}_i)}, \tag{2.107}$$

where n_c is the number of particles on each lattice site and $\vec{R}_i$ are the lattice vectors, which are generated by the basis vectors. The number of lattice vectors used with calculation should be as many as possible until the free energy is nearly unchanged when α is fixed. Then we can minimize the free energy by optimizing n_c and α. This method is widely used in the study of ultra-soft particles and solid crystals [1, 29, 59]. It usually works well if the particles are highly localized on lattice points and the symmetry of the lattice structure is simple, i.e., BCC and FCC phases. However, if we want to explore more exotic structures which have less symmetry, such as double gyroid phase and complex Frank-Kasper phases, this method becomes impractical. Therefore, an efficient minimization method is required in those situations. In this study, we employ three different numerical methods, which are the Picard iteration, the preconditioned conjugate gradient method, and the Anderson mixing method, to minimize the grand potential $\Omega(\rho)$.

The preconditioned conjugate gradient method is used in the lattice gas model and Carnahan-Starling approximation. The combination of the Picard method and Anderson mixing method is used in the FMT-WB model.

2.9.1 Preconditioned conjugate gradient

The idea of preconditioned conjugate gradient method is based on the steepest decent method. This method has been used in the study of LDA model by Pini *et al.* [39]. The density iteration scheme of steepest decent is expressed as,

$$\rho^{i+1}(\vec{r}) = \rho^{i}(\vec{r}) - \epsilon \frac{\delta\Omega}{\delta\rho(\vec{r})}\bigg|_{i}. \tag{2.108}$$

Since we are interested in periodic structure, we also need to optimize the periods of phases as well:

$$h_l^{i+1} = h_l^i - \theta \left.\frac{\partial\Omega}{\partial h_l}\right|_i \tag{2.109}$$

where ϵ and θ are the parameters controlling the step sizes. h_l is the lattice parameter. For the lattice gas model and Caranhan-starling approximation model, $\delta\Omega/\delta\rho$ are calculated analytically in equations (2.35) and (2.51). And $\partial\partial/\delta h$ is expressed as

$$\frac{\partial\Omega}{\partial h_l} = \frac{1}{2}\sum_{\vec{k}} \left|\rho(\vec{k})\right|^2 \frac{dw(k)}{dk}\frac{dk}{dh_l}. \tag{2.110}$$

The efficiency of equation (2.108) can be improved by using the Jacobi preconditioner. We can combine the preconditioner with the steepest decent method, and hence equation (2.108) is replaced by,

$$\rho^{i+1}(\vec{r}) = \rho^{i}(\vec{r}) - \eta\xi^{i}(\vec{r}), \tag{2.111}$$

where,

$$\xi^i(\vec{r}) = \frac{\delta\Omega}{\delta\rho(\vec{r})}\bigg|_i \left(\frac{\delta^2\Omega}{\delta\rho^2(\vec{r})}\bigg|_i\right)^{-1}. \tag{2.112}$$

The second order derivative of lattice gas model is given by,

$$\frac{\delta^2\beta\Omega}{\delta\rho^2(\vec{r})} = \frac{1}{V}\left(\frac{1}{\rho} + \frac{1}{\rho_m - \rho}\right) + \frac{1}{\rho_m^2 V}\omega(k=0) \tag{2.113}$$

And the second order derivative of LDA model is given by,

$$\frac{\delta^2\beta\Omega}{\delta\rho^2(\vec{r})} = \frac{1}{V}\frac{\eta^4 - 4\eta^3 + 4\eta^2 + 4\eta + 1}{\rho(\vec{r})(1-\eta)^4} + \frac{1}{V}w(k=0). \tag{2.114}$$

We can further improve the efficiency of preconditioned steepest decent method by a Newton-like approach, namely the preconditioned conjugate gradient. The density iteration equation is given by

$$\rho^{i+1}(\vec{r}) = \rho^i(\vec{r}) - \epsilon\psi^i(\vec{r}), \tag{2.115}$$

where $\psi^i(\vec{r})$ is determined by the history of $\xi^i(\vec{r})$ in the previous step and it is given by the following recurrence relations:

$$\psi^i(\vec{r}) = \xi^i(\vec{r}) + \zeta^i\psi^{i-1}(\vec{r}), \tag{2.116}$$

$$\zeta^i = \frac{\frac{1}{V}\int \xi^i(\vec{r})\left[\xi^i(\vec{r}) - \xi^{i-1}(\vec{r})\right]d\vec{r}}{\frac{1}{V}\int\left[\xi^{i-1}(\vec{r})\right]^2 d\vec{r}}. \tag{2.117}$$

Equation (2.115) is generally more efficient, but it is less robust than equation (2.108). Therefore we can perform the preconditioned steepest decent method every 50 steps after use the preconditioned conjugate gradient method. The adaptive step sizes: ϵ and θ are determined by minimizing $g^i(\epsilon, \theta)$. $g^i(\epsilon, \theta)$ is defined as,

$$g^i(\epsilon, \theta) = \frac{1}{V}\Omega\left[\rho^i(\vec{r}) - \epsilon\psi^i(\vec{r}), h_l^i - \theta\left.\frac{\partial\Omega}{\partial h_l}\right|_i\right]. \tag{2.118}$$

The minimization of $g^i(\epsilon, \theta)$ is numerically evaluated by solving the equations,

$$\begin{aligned}\frac{\partial g^i}{\partial \epsilon} &= 0,\\ \frac{\partial g^i}{\partial \theta} &= 0.\end{aligned} \tag{2.119}$$

Using the Raphson-Newton method, one can find the approximated expression for ϵ and θ [39]:

$$\epsilon^i = -\frac{\partial g^i}{\partial \epsilon}\left(\frac{\partial^2 g^i}{\partial \epsilon^2}\right)^{-1}\Bigg|_{\epsilon,\theta=0}, \tag{2.120}$$

$$\theta^i = -\frac{\partial g^i}{\partial \theta}\left(\frac{\partial^2 g^i}{\partial \theta^2}\right)^{-1}\Bigg|_{\epsilon,\theta=0}. \tag{2.121}$$

The derivatives of g^i are given by,

$$\frac{\partial g^i}{\partial \epsilon} = -\int d\vec{r} \frac{\delta \Omega}{\delta \rho(\vec{r})} \psi(\vec{r}), \tag{2.122}$$

$$\frac{\partial^2 g^i}{\partial \epsilon^2} = \int d\vec{r} \int d\vec{r}' \frac{\delta^2 \Omega}{\delta \rho(\vec{r}) \delta \rho(\vec{r}')} \psi(\vec{r}) \psi(\vec{r}'), \tag{2.123}$$

$$\frac{\partial g^i}{\partial \theta} = -\sum_l \frac{\partial \Omega}{\partial h_l} \frac{\partial \Omega}{\partial h_l}, \tag{2.124}$$

$$\frac{\partial^2 g^i}{\partial \theta^2} = \sum_l \sum_{l'} \frac{\partial^2 \Omega}{\partial h_l \partial h_{l'}} \frac{\partial \Omega}{\partial h_l} \frac{\partial \Omega}{\partial h_{l'}}. \tag{2.125}$$

Evaluation of these equations requires the first and the second order derivatives of grand potential with respect to ρ and h_l, and they are listed in the Appendix A.

2.9.2 Picard iteration

The general solution of equilibrium density profile can be written in the form:

$$\rho = \exp[\beta\mu + c^{(1)}(\vec{r})], \tag{2.126}$$

where $c^{(1)}$ is the one-body direct correlation function, which is given by,

$$c^{(1)} = -\beta \frac{\delta F^{ex}(\rho)}{\delta \rho}. \tag{2.127}$$

The numerical minimization process starts from an initial guess of the density profile. When the input density profile is still far from the true equilibrium density, directly using equation (2.126) can cause divergence issues. Therefore, we employ the Picard iteration, which is also known as simple mixing. At each iteration step, we mix ρ_{new}, which is calculated by equation (2.126), with the solution in the

previous step:

$$\rho^{i+1}(\vec{r}) = (1-\alpha)\rho^{i}(\vec{r}) + \alpha\rho_{new}(\vec{r}), \tag{2.128}$$

where α is the mixing parameter and the value is usually between 0.03 and 0.1. The value of α should be chosen such that the iteration is stable and the convergence speed is fast. The robustness is main advantage of Picard iteration, however, it becomes less efficient and even does not converge when the solution is close to the equilibrium density. Therefore new algorithms are needed to accelerate the convergence rate.

2.9.3 Anderson mixing

Several sophisticated and efficient minimization algorithms are available for solving large non-linear systems. For example, Roth *et al.* applied the limited memory inverse Broyden algorithm to the free-minimization of FMT-WB [8]. The limited memory inverse Broyden algorithm is a quasi-Newton method which has super-linear convergence speed, and it only needs a small amount of memory. However, due to the structure of the algorithm, it is hard to combine this method with modern parallel programming technology, such as Open MP. Here we introduce the Anderson mixing (AM) algorithm, which is simpler, more efficient, and parallel computing-friendly. AM is a type of fixed-point iteration method used to solve non-linear systems such as $f(x_i) = x_i$. It is widely used in self-consistent field theory [50, 53]. Unlike the simple mixing, which only uses the information from the previous step, AM combines the information from several previous steps and

predicts the next step, for example:

$$\rho^{i+1} = (1 - \lambda_1 - \lambda_2 ..... \lambda_j) f(\rho^i) + \lambda_1 f(\rho^{i-1}) + \lambda_2 f(\rho^{i-2}) + ... \lambda_j f(\rho^{i-j+1}) \quad (2.129)$$

Then the problem is how to determine suitable value for each λ_j. Here we define the residual function at each iteration step i:

$$d^i(\vec{r}) = f(\rho^i(\vec{r})) - \rho^i(\vec{r}), \quad (2.130)$$

and the inner product of functions:

$$\langle f(\vec{r}), g(\vec{r}) \rangle = \int d\vec{r} f(\vec{r}) g(\vec{r}). \quad (2.131)$$

Then, the total deviation of density at step i is given by,

$$d_i^{total} = \left| \frac{\langle d_i(\vec{r}), d_i(\vec{r}) \rangle}{\langle \rho^i(\vec{r}), \rho^i(\vec{r}) \rangle} \right|^2. \quad (2.132)$$

Then we define a $n \times n$ matrix U, and its elements are given by,

$$U_{nm} = \langle d^i \vec{r} - d^{i-n}(\vec{r}), d^i \vec{r} - d^{i-m}(\vec{r}) \rangle, \quad (2.133)$$

where n is the number of history steps we used. And we define a vector:

$$V_n = \langle d^i(\vec{r}) - d^{i-n}(\vec{r}), d^i(\vec{r}) \rangle, \quad (2.134)$$

The mixing coefficients λ_i are given by the solution of system:

$$U_{mn}\lambda_n = V_n. \tag{2.135}$$

And hence we have the expression for Anderson mixing:

$$\rho^{i+1}(\vec{r}) = f(\rho^i) + \sum_n \lambda_n (f(\rho^{i-n}) - f(\rho^i)), \tag{2.136}$$

In practice, we use the simple mixing method at the beginning when the solution is far away from equilibrium density. When $d^{total} < 10^{-4}$ is satisfied, we switch to the Anderson Mixing until certain convergence condition is reached. To balance the efficiency and accuracy of algorithm, we normally store 30 history steps. The method can be used to optimize the periods of phases as well.

2.9.4 Space discretization and phase initialization

Since we are interested in periodic structures, we take advantage of the fast Fourier transform instead of using the real space method. The computation is performed within a simulation box with dimensions: $L_x \times L_y \times L_z$ which match the periods of each phase. The first step is to discrete the box space with a number of point: $N = N_x N_y N_z$, and the unit volume $v = \frac{\Delta L_x}{N_x}\frac{\Delta L_y}{N_y}\frac{\Delta L_z}{N_z} = L_x L_y L_z / N$. Then the value of density function within each unit volume labeled by vector r_{abc} is represented by the $\rho(r_{ijk})$. The vector r_{abc} is given by $r_{abc} = a\Delta L_x \hat{i} + b\Delta L_y \hat{j} + c\Delta L_z \hat{k}$, and $a = 0...N_x - 1, b = 0...N_y - 1, c = 0...N_z - 1$. The discretization numbers are different for different phases, and they are listed in the Appendix B table 5.1.

The discretization in real space also defines the frequencies of discrete Fourier transform. The maximum frequency is determined by grid spacing: $f^{\alpha}_{\max} = \frac{2N_{\alpha}\pi}{L_x}$, here α is the x,y,z-direction. Which means that we use dozens of low frequency modes and ignore very high frequency modes. In this case, the density distribution should not vary too abruptly. The resulting discrete Fourier transform is given by,

$$\hat{\rho}_{nml} = \frac{1}{N} \sum_{n,l,m} \rho(\vec{r}_{abc}) \exp(i\vec{k}_{nml} \cdot \vec{r}_{abc}), \tag{2.137}$$

where n, m, l are integers: $(-\frac{N_x}{2}) + 1 \leqslant n \leqslant \frac{N_x}{2}$, $(-\frac{N_y}{2}) + 1 \leqslant m \leqslant \frac{N_y}{2}$, $(-\frac{N_z}{2}) + 1 \leqslant l \leqslant \frac{N_z}{2}$.

We need to initialize the interested phases. For the lamella phase, we use a simple cosine function as the initial guess. For the double gyroid and the hexagonal phases, we use two-shell approximation. For the rest of phases: BCC, FCC, HCP, σ, A15 as well as inverted phases, we firstly specify the coordination and radius of micelles in terms of box size. Then, the density of micelles is assumed to be isotropic and follow the Gaussian distribution along radial direction. Therefore we can generate the initial density profiles for different phases. The exact coordination of micelles and radius can be found in Appendix B. Here, we plot the density distribution of the initial phases in Figure 2.2.

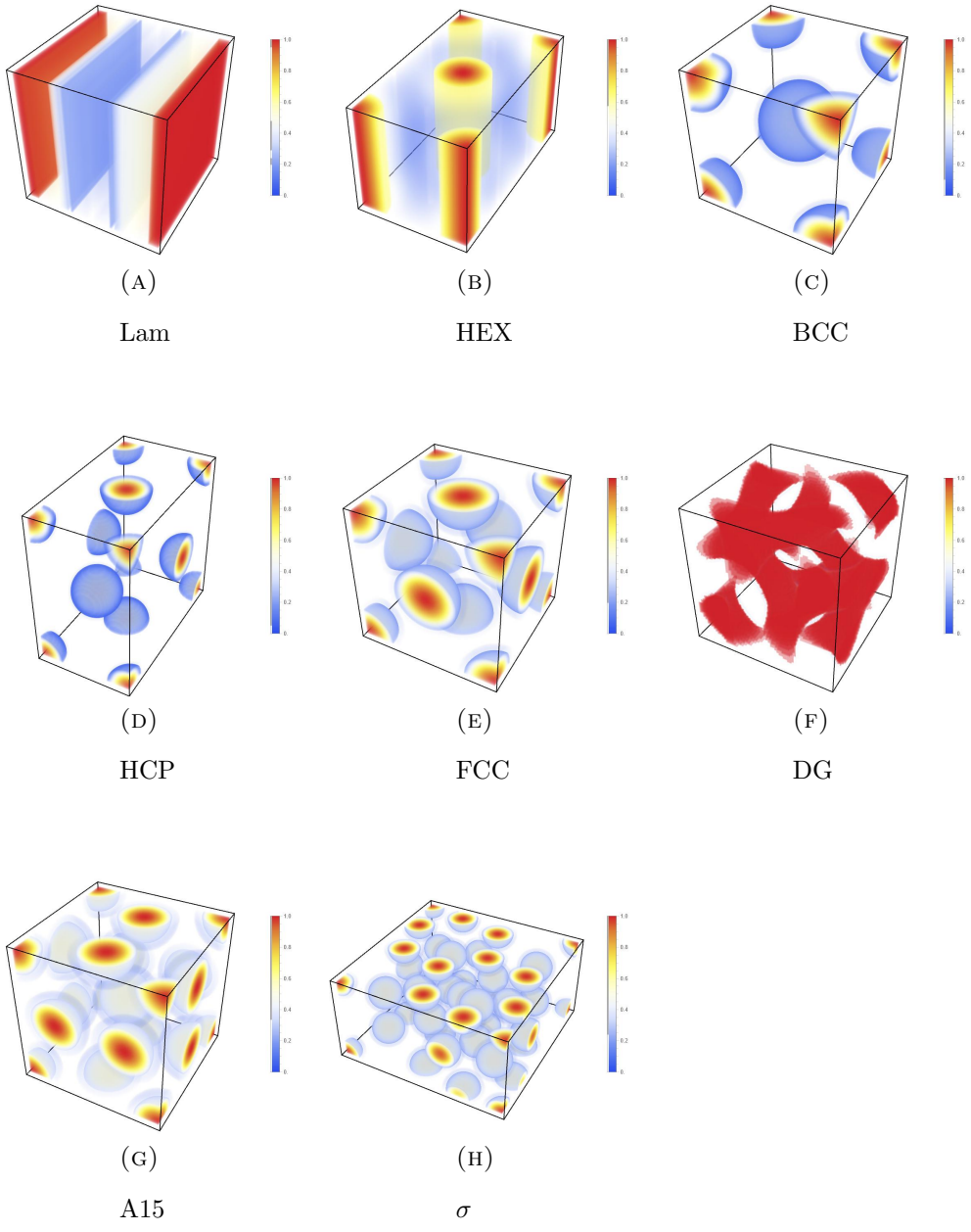

(A) Lam (B) HEX (C) BCC

(D) HCP (E) FCC (F) DG

(G) A15 (H) σ

FIGURE 2.2: The density distribution functions of eight order phases that are used as initial inputs for lattice gas model and LDA model.

2.9.5 Phase diagram Construction

In this section, we present the methodology for constructing phase diagrams utilizing density functional theory. The construction of the phase diagram is achieved through the calculation of the grand potential in the grand canonical ensemble. The grand potential depends on two variables: chemical potential μ and scaled temperature kT/ϵ. We are interested in the minimum grand potential at the fixed μ and the scaled temperature. First of all, we compute the grand potentials for different phases as a function of chemical potential and average density at a given temperature. Then we interpolate those grand potentials as a function of chemical potential via the spline algorithm and find the phase with the minimum grand potential within a certain range of μ. For example, in Figure (2.3), we plot the grand potential differences of candidate phases and find that HCP has the minimum grand potential when $\mu < -1.66865$, whereas σ becomes stable when $\mu > -1.66865$. The intersection gives the critical chemical potential μ_c of two-phase coexistence. Since the phase diagrams are presented on the $T - \rho$ plane, the next step is to find the average densities of HCP (ρ_a) and σ (ρ_b) phases at μ_c. Here we interpolate the average density $\rho(\mu)$ for two phases as a function of μ, and hence we can find ($\rho_a(\mu_c)$) and ($\rho_b(\mu_c)$). The two average densities give the coexistence boundary of the two phases. By repeating this process at different temperatures, we obtained a set of discrete points for phase boundaries. Finally, we interpolate those points as a function of temperature via the cubic algorithm and generate the phase diagrams. Also, we ignore the two-phase coexistence region if it is too small, i.e., $|\rho_a(\mu_c) - \rho_b(\mu_c)| \leqslant 0.005$.

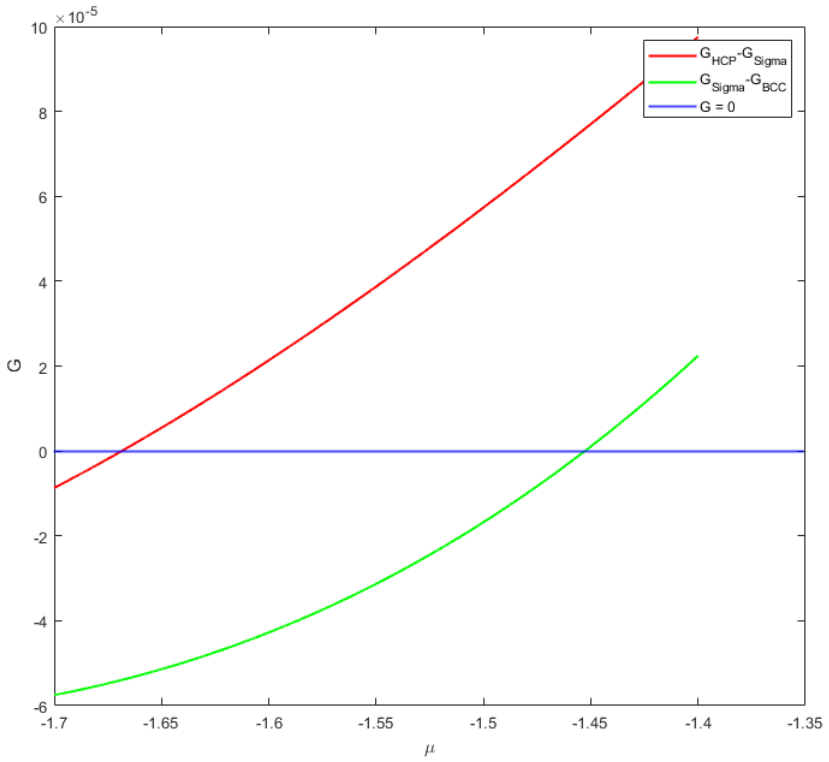

FIGURE 2.3: The plot of grand potential differences: $G_{\mathrm{HCP}} - G_{\sigma}$ (red), $G_{\sigma} - G_{\mathrm{BCC}}$(green) and $G = 0$ (blue). The horizontal axis is chemical potential μ and the vertical axis is the grand potential G. The red curve intersect with the horizontal line $G = 0$ at critical chemical potential $\mu = -1.66865$, indicating the boundary of HCP and σ phases coexistence region.

Chapter 3

Results and Discussion

3.1 Overview of phase diagrams

In this section, we present the phase diagrams obtained for the three different hard-sphere models with two generic double Gaussian potentials. In order to make direct comparison, the phase diagrams are presented in the $T/T^* - \bar{\rho}$ plane with the temperature T rescaled by the critical temperature T^*. The unit of temperature is $\frac{kT^*}{\epsilon}$ and $\bar{\rho} = \rho\sigma^3$ is the reduced density. The red horizontal lines in each phase diagrams are the computation boundaries.

The calculated phase diagrams are shown in Figure 3.1, for the three different models interacting via generic Double Gaussian 1 (GDG1) and generic Double Gaussian 2 (GDG2) potentials. In the six phase diagrams, we can see a universal phase transition sequence: spherical phase → cylindrical phase → double gyroid → lamellar → inverse phases as the average density increases. For the GDG1 potential, when $\bar{\rho} < 0.2$ and $T/T^* < 0.83$, the HCP phase is predicted to be stable for all three models. In the high temperature region, the BCC phase becomes stable. As the average density increases, the stable phase changes from hexagonal phase

to double gyroid phase and then to lamella phase, where the double gyroid phase is missing if the temperature is high enough (i.e. $T/T^* \geqslant 0.85$). The phase diagrams with the GDG2 potential demonstrate similar behavior. However, the details of phases diagrams generated by different models differ considerably. For the lattice gas model, the phase diagram is symmetric about $\rho = 0.5$ which comes form the fact that each lattice site can only be occupied by one particle or remain empty. Whereas the phase diagrams predicted by the LDA and the FMT-WB models are all asymmetric. More interestingly, there are stability widows of the FK phases in all these phase diagrams. Specifically, in all six phase diagrams, the σ and the inverse σ phases have stability windows on the low and high density regions, respectively, despite that the location and area of these windows are sightly different in different diagrams. Moreover, the (inverse) σ phase always appears between the (inverse) BCC and the (inverse) HCP phases. For the GDG2 potential, in addition to the σ phase, the A15 phase emerges in the region between the HCP and the σ phases in the LDA model and the FMT-WB model, but the inverse A15 phase is absent, In contrast, both the A15 and the inverse A15 are only meta-stable in the lattice gas model.

3.2 The stabilization of sigma and A15 phases in hard-sphere models

We have seen that the phase behaviour of the systems, especially the formation of the FK phases, is sensitively dependent on the inter-particle interaction potentials. In this section, we focus on understanding the effect of the form of the interaction potential on the stability of the FK phases in more details. In order to understand

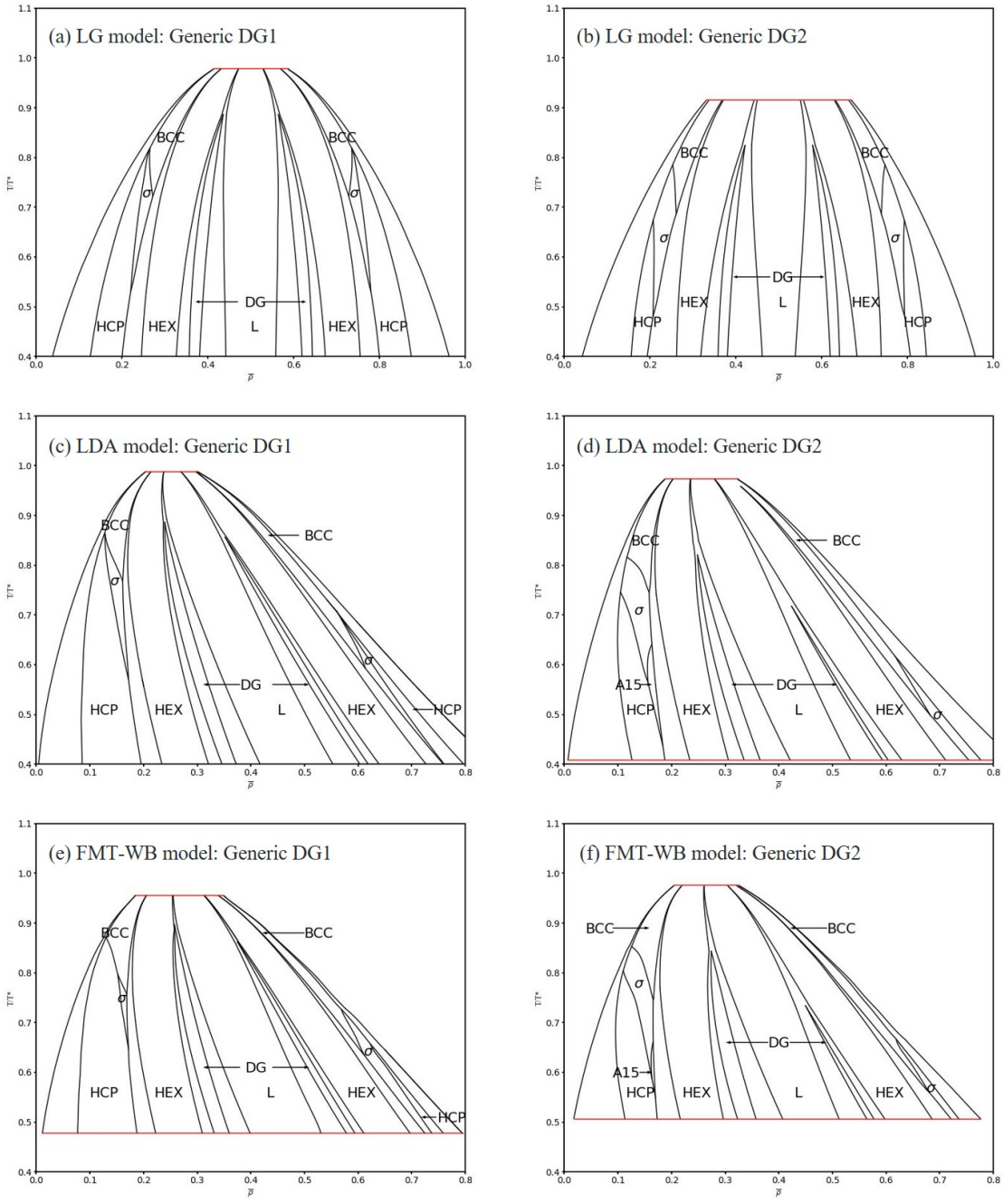

FIGURE 3.1: The phase diagrams generated by three hard-sphere models with two SALR potentials. The overall phase diagrams are normalized by its critical temperature. The red horizontal lines indicate the temperature boundaries.

how the inter-particle potentials affect the formation of the Frank-Kasper phases in different theoretical models of hard spheres, we make connection between the current density functional theories to the Ginzburg-Landau (GL) theories. The GL theories assumes that the free energy functional is a functional of order parameter $\phi(\vec{r})$. The order parameter $\phi(\vec{r}) = 0$ in the disorder phase, and its magnitude should not become too large in the ordered phases. Thus we can perform Taylor expansion for the free energy functional [7]:

$$F[\phi(\vec{r})] = \sum_{n=2}^{\infty} \frac{1}{n!} \int d\vec{r}_1 ... d\vec{r}_n G_n(\vec{r}_1 ... \vec{r}_n)\phi(\vec{r}_1)...\phi(\vec{r}_n), \tag{3.1}$$

where G_n are the undetermined constants. Then we use the translation invariance property of the system and Fourier transform, the second order term can be simplified to,

$$F_2[\phi(\vec{r})] = \frac{1}{2} \int \frac{d\vec{q}}{(2\pi)^3} G_2(\vec{q})\phi(\vec{q})\phi(-\vec{q}), \tag{3.2}$$

where $G_2(\vec{q})$ and $\phi(\vec{q})$ are the Fourier transformation of $G_2(r)$ and $\phi(r)$. We truncate the expansion up to the fourth order, and hence we have the following expression:

$$F[\phi(\vec{r})] = \frac{1}{2} \int \frac{d\vec{q}}{(2\pi)^3} G_2(\vec{q})\phi(\vec{q})\phi(-\vec{q}) + \int d\vec{r} \left\{ \frac{G_3}{3!}\phi(\vec{r})^3 + \frac{G_4}{4!}\phi(\vec{r})^4 \right\}. \tag{3.3}$$

The GL theory is a simple yet powerful tool to study the phase transition behaviour. Different types of models have been developed by tuning the coefficients G_i, such as Landau-Brazovskii (LB) model and Ohta-Kawaski (OK) model. Duncan McClenegan and Sarah Dawson have studied the formation of the Frank-kasper phases in those models [7, 27]. Specifically, it has been revealed that the formation

of Frank-Kasper phases is promoted by the low free energy cost associated with the long wavelength modes and suppressed by the low free energy cost associated with the short wavelength modes. Although we cannot completely separate the free energy contribution of long and short wavelength modes in the current DFT models, because of the non-linear entropic term in the free energy functional, we could compare the free energy cost of different modes due to the inter-particle potentials. In the current DFT models, the mean-field free energy cost is given by,

$$f_{\mathrm{MF}} = \frac{1}{2}\sum_{k} |\rho(k)|^2 U(k), \tag{3.4}$$

where $\rho(k)$ and $U(k)$ are the Fourier transform of density distribution $\rho(r)$ and inter-particle potential $U(r)$, respectively. In order to make a direct comparison between potentials, we introduce a rescaled potential $U_N(k)$ via the expression [7]:

$$U_N(k) = \frac{2}{k_0^2 U''(k_0)} \left[U(kk_0) - U(k_0)\right], \tag{3.5}$$

where k_0 is the k value when $U(k)$ reaches its global minimum. Equation (3.5) shifts the global minimums of different potentials on $k/k_0 = 1$, and the second order derivative is normalized at this point.

In order to have a more systematic comparison, we compare our results with the phase diagrams computed by Mr.Xie and Mr.Burns [14]. The inter-particle potentials they used are the double Gaussian and the generic step which we are going to discuss here. Unlike the generic double Gaussian potentials, the centers of double Gaussian potential (DG) are located at the origin, which is given by the

expression:

$$U(r) = -Ae^{-r^2/\sigma_1^2} + Be^{-r^2/\sigma_2^2}, \tag{3.6}$$

where the parameters are defined as: $\sigma_1 = 1$, $\sigma_2 = 1.4$, $A = 2.744$, $B = 1$. The generic step potential (GS) has a slightly complex expression:

$$U(r) = A_1\Theta(r)\Theta(1-r) - A_2\Theta(r-1)\Theta(1-(r-1)) + (-\frac{r}{3}+\frac{7}{6})\Theta(r-\frac{4}{3})\Theta(1-\frac{r-2}{3/2}), \tag{3.7}$$

where Θ is the Heaviside step function and $A_1 = 5, A_2 = 4.265$. It is noted that these two forms of potentials also have SALR characteristic.

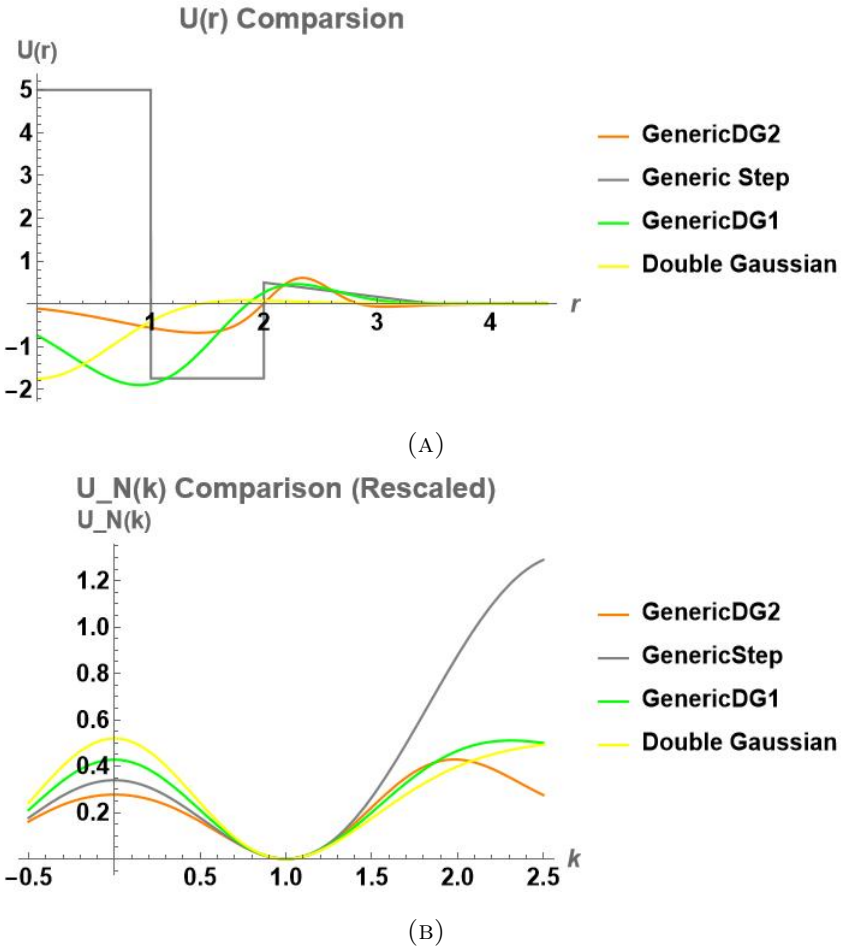

FIGURE 3.2: Four SALR potentials in the real space and the corresponding rescaled potentials in the Fourier space are plotted in (A) and (B) respectively.

In Figure 3.2, we plot all four potentials $U(r)$ in the real space and the corresponding rescaled potentials $U_N(k)$ in the Fourier space. In Figure 3.2 (B), we observe that the magnitude of potentials follow the order: $U_{\mathrm{GDG2}}(k) < U_{\mathrm{GS}}(k) < U_{\mathrm{GDG1}}(k) < U_{\mathrm{DG}}(k)$ when k is less then one, which is correlated to the order of the free energy cost due to long wavelength modes. Therefore, the formation of

Frank-Kasper phases should be favored by the GDG2 potential most. If we focus on the short wavelength modes, i.e. $1 < k < 1.7$, the order of free energy cost is $U_{\mathrm{GS}}(k) > U_{\mathrm{GDG2}}(k) > U_{\mathrm{GDG1}}(k) > U_{\mathrm{DG}}(k)$. Thus in terms of short wavelength modes, the formation of Frank-Kasper phases should be favored by the GS potential most. When $k > 1.7$, three potentials (GDG2, GDG1 and DG) have intersections, which makes it hard to compare their contributions. However, we anticipate that the free energy contribution of those high-frequency modes ($k > 1.7$) is less significant than other high-frequency modes.

Now we can examine how those different potentials affect the stabilization of Frank-Kasper phases in different models. In Figure 3.3, we plot the phase diagrams of lattice gas model for four different potentials. We compare the areas of stable region of the σ phase, and find the areas follow the order: $A_{\mathrm{GDG2}} > A_{\mathrm{GS}} > A_{\mathrm{GDG1}} > A_{\mathrm{DG}}$, which is the same as the order of free energy cost associated with long wavelength modes. However, the A15 phase is only stable in the generic step potential. This observation implies that the stabilization of the σ phase is more sensitive to the free energy cost of long wavelength modes ($0 < k < 1$), whereas the stabilization of A15 phase is more sensitive to the free energy cost of short wavelength modes ($1.7 > k > 1$) in the lattice gas model.

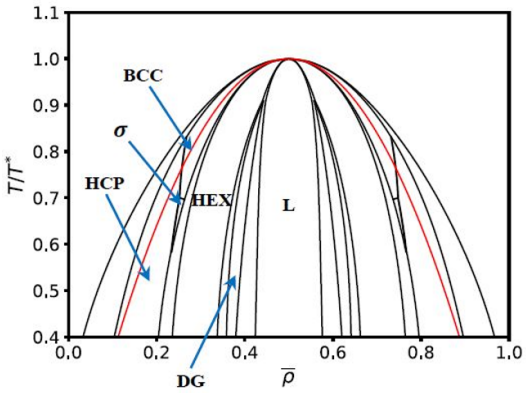

(A) Double Gaussian

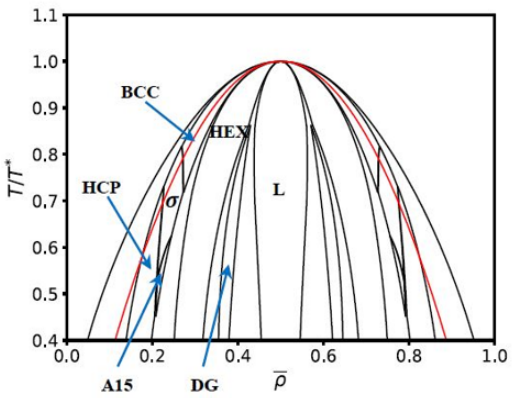

(B) Generic Step

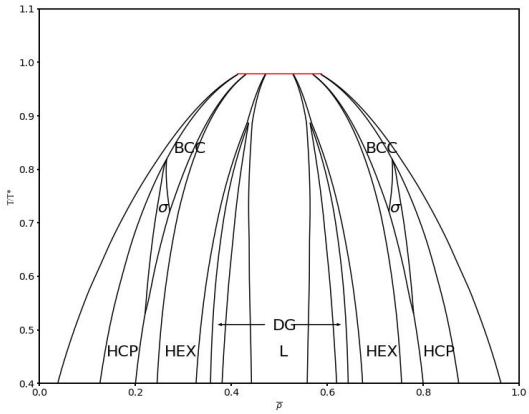

(C) Generic DG1

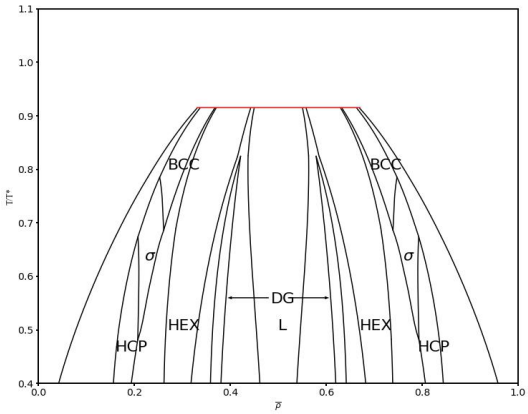

(D) Generic DG2

FIGURE 3.3: The phase diagrams of lattic gas model generated by four different potentials:(A) Double Gaussian (DG), (B) Generic Step (GS), (C) Generic DG1 (GDG1), (D) Generic DG2 (GDG2). The first two figures (A) and (B) are reproduced from the reference [14].

We turn to the phase diagrams of the LDA model for different potentials. Obviously, the areas of stable region of the σ phase still follow the same order as in the lattice gas model,i.e. $A_{\mathrm{GDG2}} > A_{\mathrm{GS}} > A_{\mathrm{GDG1}} > A_{\mathrm{DG}}$. Interestingly, we find that the A15 phase is stable in the phase diagrams of the GS and GDG2 potentials.

Moreover, the areas of its stable regions are nearly the same in the GDG2 and GS potentials. From these observations, we conclude that the σ phase and A15 phase are more sensitive to the free energy cost of long wavelength modes in the LDA model. In other words, the A15 phase in the LDA model is less sensitive to the free energy cost of short wavelength modes than the A15 phase in the lattice gas model.

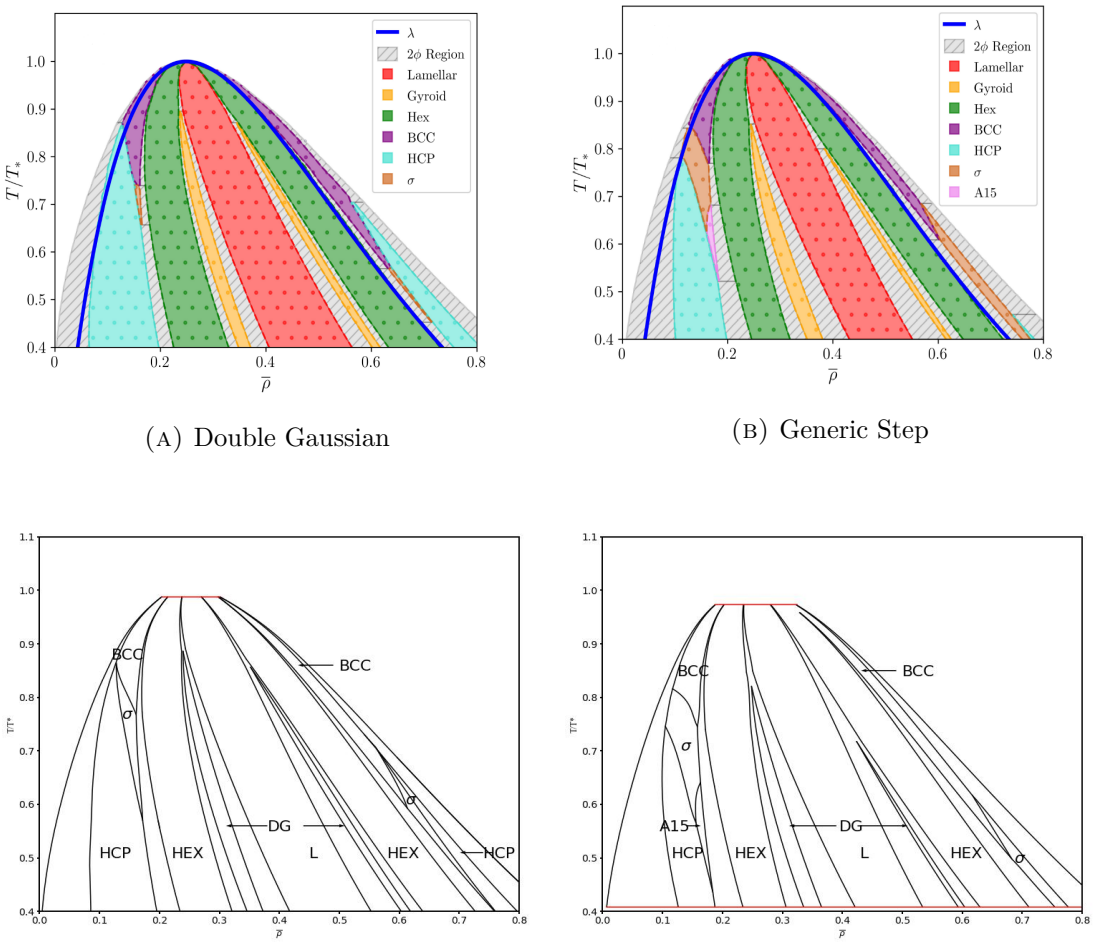

(A) Double Gaussian

(B) Generic Step

(C) Generic DG1

(D) Generic DG2

FIGURE 3.4: The phase diagrams of LDA model generated by four different potentials: (A) Double Gaussian (DG), (B) Generic Step (GS), (C) Generic DG1 (GDG1), (D) Generic DG2 (GDG2). The first two figures (A) and (B) are reproduced from the reference [14].

In the case of the FMT-WB model, it is observed that the phase diagram topology exhibits a high degree of similarity to those of the LDA model with the same inter-particle potentials. For the GDG1 potential, the relative stable region of the σ phase in the FMT-WB model is significantly smaller than that of the σ

phase in the LDA model. With the GDG2 potential, both models predict stable σ and A15 phases windows at similar regions in the phase diagrams. Upon comparing the phase diagrams of the FMT-WB and LDA models, it can be concluded that, despite of minor shifts in the phase boundaries, the DFT theories based on local-density approximation and weighted-density approximation produce strikingly similar phase diagrams. As previously mentioned, the FMT-WB model allows us to access the internal structure of clusters, namely the local packing effect. We demonstrate this effect by plotting the density profile of the BCC phase along a spatial line in the FMT-WB model. The spatial line is chosen to be parallel to the x-axis and pass the center of the central cluster of BCC phase. We plot the density distributions on this line at different scaled temperatures in Figure (3.5). It could be seen that when the temperature is low, the interface of the FMT-WB model (dashed line) becomes sharper and the local packing effect is more pronounced. In contrast, the cut-through density profile of the BCC structure for the LDA model (solid line) demonstrates a smoother interface. This local packing effect is also evident in all other phases, which is shown in Appendix C.

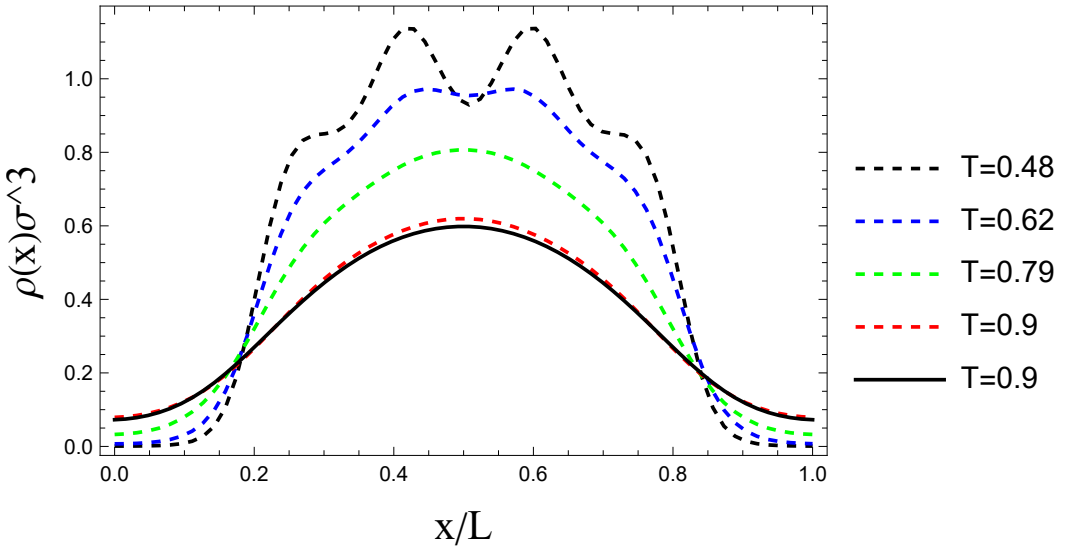

FIGURE 3.5: The BCC phase density profiles for the FMT-WB model (Dashed line) and the LDA model (Solid line) at different temperatures. L is the period of BCC phase. The local packing effect is visible at lower temperature in the FMT-WB model.

In polymeric blending systems, i.e., asymmetric AB/AB diblock copolymer mixtures [56] and AB/A copolymer mixtures [57], different Frank-Kasper phases, including σ, A15, C14, and C15 phases, have been found to be stable. In these systems, polymeric domains created by minority blocks inevitably deviate from perfect sphericity as they increase in size, owing to their deformation toward the shape of the corresponding Wigner-Seitz cell (WSC). This deformation results additional free energy plenty and hence the WSCs which have more spherical shapes are enthalpically favoured. It is believed that the formation of Frank-Kasper phases are favored when the domains are enlarged and the phase transition to the HEX phase is prevented. This is attribute to the fact that their Wigner-Seitz cells, on average, retain a more spherical shape in comparison to those of the BCC and the HCP structures [41, 19]. Therefore, we compute the volume ratio (V/V_{WSC}) between clusters and Wigner-Seitz cells for BCC, HCP, σ, and A15 phases in the

LDA model and the Lattice gas model. The boundary of a cluster is defined as where the density $\rho(\vec{r})$ equals the average density $\bar{\rho}$. In Figure 3.6, we plot the ratios computed with the four different potentials for the lattice gas model Figure 3.6 (A) and those for the LDA model in Figure 3.6 (B). On the x-axis, the potentials from left to right are in an ascending order of the area of the stability window of the Frank-Kasper phases. We can clearly see a positive correlation for all the nonequivalent cluster except for one cluster of the A15 phase. This trend of the particle size observed in the current hard-sphere system is similar to that observed polymeric systems, which may suggest similarities in the mechanisms stabilizing the FK phase in these two different soft matter systems.

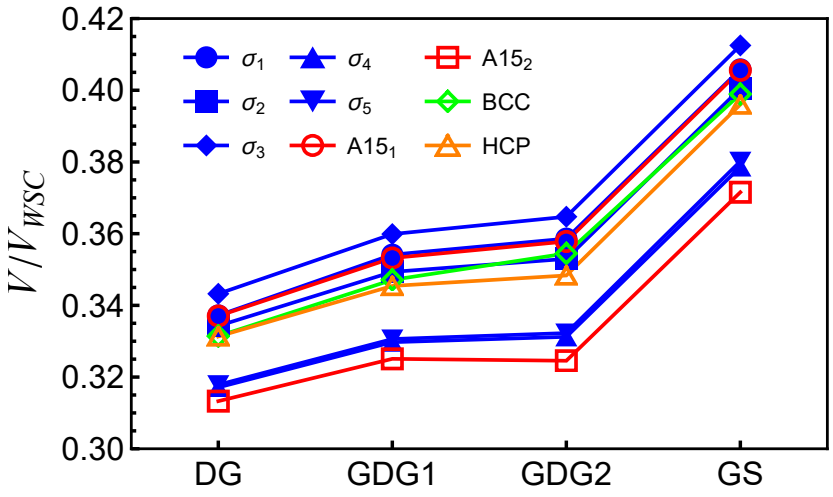

(A)

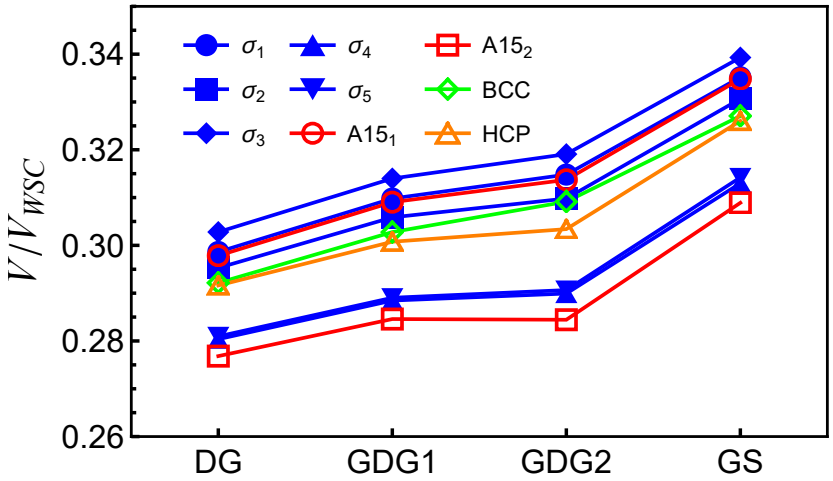

(B)

FIGURE 3.6: The volume ratios between the clusters and their Wigner-Seitz cells for four types of phases: BCC, HCP, σ and A15 in LG model (a) and LDA model (b). The potentials on x-axis are arranged in ascending order of areas of Frank-Kasper phases stability windows: $A_{\mathrm{DG}} < A_{\mathrm{GDG1}} < A_{\mathrm{GDG2}} \approx A_{\mathrm{GS}}$.

Chapter 4

Conclusion

4.1 Conclusion

In this study, phase diagrams for three hard-sphere models, namely the lattice gas model, LDA model, and FMT-WB model, were constructed using two SALR potentials. It was demonstrated that the generic phase transition sequences are consistent across the different models and potentials. A comparison was made between our phase diagrams and previous work conducted by Xie, Dawson, and Burns. The stability of the Frank-Kasper phases, namely the σ and A15 phases, was confirmed in all three models. The emergence of Frank-Kasper phases in hard-sphere models was found to be strongly correlated with the mean-field free energy contributions of long and short wavelength modes. This research marks the first instance in which complete phase diagrams of fundamental measure theory have been computed, revealing the presence of the σ and A15 phases. A comparative analysis illustrated that the phase topology of the FMT-WB model and LDA model is similar, with slight shift in phase boundaries. The results obtained from the current study clearly demonstrate the universality of the phase behaviour of self-assembly colloidal systems, and shed light on understanding the formation of

complex phases in soft matter. Desipte these progress, a fundamental physical interpretation of the stabilization of Frank-Kasper phases in hard-sphere systems remains unclear, providing a potential direction for future investigation.

Chapter 5

Appendices

5.1 Appendix A

Numerical Minimization Methods

Since we are interested in periodic structure, we minimize the grand potential with respect to density $\rho(\vec{r})$ and period h_l simultaneously via $\delta\beta\Omega/\delta\rho$ and $\delta\beta\Omega/\delta h_l$. The exact expressions could be different, but $\delta\beta\Omega_{\rm ex}^{\rm MF}/\delta h_l$ are the same for three models and it is given below:

$$\frac{\partial\beta\Omega_{\rm ex}^{\rm MF}}{\partial h_l} = \frac{1}{2}\sum_{\vec{k}}\frac{d\omega(k)}{dk}\frac{dk}{dh_l}, \tag{5.1}$$

where $\omega(k)$ is spherically symmetric and $k = \sqrt{k_x^2 + k_y^2 + k_z^2}$.

$$\frac{dk}{dh_l} = \frac{dk}{dk_l}\frac{dk_l}{dh_l} = -\frac{1}{h_l}\frac{k_l^2}{k}. \tag{5.2}$$

The preconditioned conjugated gradient method also requires the second order derivative:

$$\frac{\partial^2\beta\Omega_{\rm ex}^{\rm MF}}{\partial h_l \partial h_{l'}} = \frac{1}{2}\sum_{\vec{k}}\left|\rho(\vec{k})\right|^2\left[\frac{d^2w(k)}{dk^2}\frac{dk}{dh_l}\frac{dk}{dh_{l'}} + \frac{dw(k)}{dk}\frac{d^2k}{dh_l dh_{l'}}\right], \tag{5.3}$$

where,

$$\frac{\partial^2 k}{\partial {h_l}^2} = \frac{1}{{h_l}^2}\frac{3k_l^2k^2 - k_l^4}{k^3}, \tag{5.4}$$

$$\frac{\partial^2 k}{\partial h_l \partial h_{l'}} = -\frac{1}{h_l h_{l'}}\frac{k_l^2 k_{l'}^2}{k^3}. \tag{5.5}$$

The period can be optimized by the methods introduced in the algorithm section.

Lattice gas model

The minimization process requires the quantity $\delta^2(\beta\Omega)/\delta\rho^2$:

$$\frac{\delta^2\beta\Omega}{\delta\rho^2(\vec{r})} = \frac{1}{V}\left(\frac{1}{\rho(\vec{r})} + \frac{1}{\rho_m - \rho(\vec{r})}\right) + \frac{\beta}{\rho_m^2 V}\omega(k)_{\text{mini}}. \tag{5.6}$$

And hence one can find $\partial^2 g^i/\partial\epsilon^2$:

$$\frac{\partial^2 g^i}{\partial\epsilon^2} = \frac{1}{V}\int d\vec{r}\left[\frac{1}{\rho(\vec{r})} + \frac{1}{\rho_m - \rho(\vec{r})}\right] + \sum_{\vec{k}} w(k)\left|\psi(\vec{k})\right|^2. \tag{5.7}$$

Local density approximation model

$$\frac{\delta^2\beta\Omega}{\delta\rho^2(\vec{r})} = \frac{1}{V}\frac{\eta^4 - 4\eta^3 + 4\eta^2 + 4\eta + 1}{\rho(\vec{r})(1-\eta)^4} + \frac{1}{V}w(k=0) \tag{5.8}$$

$$\frac{\partial^2 g^i}{\partial\epsilon^2} = \frac{1}{V}\int d\vec{r}\left[\frac{(\eta^4 - 4\eta^3 + 4\eta^2 + 4\eta + 1)}{\rho(\vec{r})(1-\eta)^4}\psi^2(\vec{r})\right] + \sum_{\vec{k}} w(k)\left|\psi(\vec{k})\right|^2 \tag{5.9}$$

FMT-WB

From equation (2.102), we need to calculate the quantities $\delta\beta\Omega_{ex}^{HS}/\delta\rho$ and $\delta\beta\Omega_{ex}^{MF}/\delta\rho$ respectively. The derivation is given here.

$\delta\Omega_{\mathbf{ex}}^{\mathbf{HS}}/\delta\rho$

The expression can be expanded as

$$\begin{aligned}\frac{\delta\beta\Omega_{\mathrm{ex}}^{\mathrm{HS}}[n_l(\vec{r}_1)]}{\delta\rho(\vec{r})} =& \sum_l \int d\vec{r}_2 \frac{\delta\Omega_{\mathrm{ex}}^{\mathrm{HS}}[n_l(\vec{r}_1)]}{\delta n_l(\vec{r}_2)} \frac{\delta n_l(\vec{r}_2)}{\delta\rho(\vec{r})} \\ =& \frac{1}{V}\sum_l \int d\vec{r}_2 T_l(\vec{r}_2) \frac{\delta n_l(\vec{r}_2)}{\delta\rho(\vec{r})},\end{aligned} \tag{5.10}$$

where l labels the six weight functions in FMT-WB. And $T_l(\vec{r}_2) = V\frac{\delta\beta\Omega_{\mathrm{ex}}^{\mathrm{HS}}[n_l(\vec{r}_1)]}{\delta n_l(\vec{r}_2)}$, are given by,

$$\begin{aligned}T_3 = \frac{\delta\Omega_{\mathrm{ex}}^{\mathrm{HS}}}{\delta n_3} =& \left\{ \frac{n_0}{1-n_3} + \frac{n_1 n_2 - \vec{n}_{V1}\cdot\vec{n}_{V2}}{(1-n_3)^2} \right. \\ &\left. + \frac{n_2^3 - 3n_2\vec{n}_{V2}\cdot\vec{n}_{V2}}{36\pi n_3^2}\left[-\frac{1}{1-n_3} - \frac{2\ln(1-n_3)}{n_3} + \frac{3n_3-1}{(1-n_3)^3}\right]\right\},\end{aligned} \tag{5.11}$$

$$T_2 = \frac{\delta\Omega_{\mathrm{ex}}^{\mathrm{HS}}}{\delta n_2} = \left\{ \frac{n_1}{1-n_3} + \frac{3n_2^2 - 3\vec{n}_{V2}\cdot\vec{n}_{V2}}{36\pi}\left[\frac{\ln(1-n_3)}{n_3^2} + \frac{1}{n_3(1-n_3)^2}\right]\right\}, \tag{5.12}$$

$$T_1 = \frac{\delta\Omega_{\mathrm{ex}}^{\mathrm{HS}}}{\delta n_1} = \left\{ \frac{n_2}{1-n_3} \right\}, \tag{5.13}$$

$$T_0 = \frac{\delta\Omega_{\rm ex}^{\rm HS}}{\delta n_0} = \{-\ln(1-n_3)\}\,, \tag{5.14}$$

$$\vec{T}_{V2} = \frac{\delta\Omega_{\rm ex}^{\rm HS}}{\delta \vec{n}_{V2}} = \left\{-\frac{\vec{n}_{V1}}{1-n_3} + \frac{-6n_2\vec{n}_{V2}}{36\pi}\left[\frac{\ln(1-n_3)}{n_3^2} + \frac{1}{n_3(1-n_3)^2}\right]\right\}, \tag{5.15}$$

$$\vec{T}_{V1} = \frac{\delta\Omega_{\rm ex}^{\rm HS}}{\delta \vec{n}_{V1}} = \left\{-\frac{\vec{n}_{V2}}{1-n_3}\right\}, \tag{5.16}$$

and $\frac{\delta n_l(\vec{r}_2)}{\delta\rho(\vec{r})}$ is given by,

$$\begin{aligned}\frac{\delta n_l(\vec{r}_2)}{\delta\rho(\vec{r})} =& \int d\vec{r}' \frac{\delta\rho(\vec{r}')}{\delta\rho(\vec{r})}\omega_l(\vec{r}_2-\vec{r}') \\ =& \int d\vec{r}'\delta(\vec{r}'-\vec{r})\omega_l(\vec{r}_2-\vec{r}') \\ =& \omega_l(\vec{r}_2-\vec{r}).\end{aligned} \tag{5.17}$$

Combining all the terms, we have,

$$\begin{aligned}\frac{\delta\beta\Omega_{\rm ex}^{\rm HS}[n_l(\vec{r}_1)]}{\delta\rho(\vec{r})} =& \frac{1}{V}\sum_l \int d\vec{r}_2 T_l(\vec{r}_2)\omega_l(\vec{r}_2-\vec{r}) \\ =& \frac{1}{V}\sum_l \mathcal{F}^{-1}\left\{T_l(\vec{k})\omega_l(k)\right\}.\end{aligned} \tag{5.18}$$

Since the Fourier transform is a linear operation, the above expression can be further simplified to,

$$\frac{\delta\beta\Omega_{\text{ex}}^{\text{HS}}[n_l(\vec{r}_1)]}{\delta\rho(\vec{r})} = \frac{1}{V}\mathcal{F}^{-1}\left\{\sum_l T_l(\vec{k})\omega_l(k)\right\}. \tag{5.19}$$

Here we need to calculate the Fourier transform of weight functions. They can be find via equation (2.14):

$$\begin{aligned}
\omega_3(\vec{k},R) &= = \frac{4\pi}{k^3}\left(\sin\left(kR_i\right) - kR_i\cos\left(kR_i\right)\right),\\
\omega_2(\vec{k},R) &= \frac{4\pi R_i}{k}\sin\left(kR_i\right),\\
\omega_1(\vec{k},R) &= \frac{1}{k}\left(\sin\left(kR_i\right)\right),\\
\omega_0(\vec{k},R) &= \frac{1}{4\pi R_i^2 k}\sin\left(kR_i\right),\\
\vec{\omega}_{V2}(\vec{k},R) &= i\vec{k}\omega_3(\vec{k},R),\\
\vec{\omega}_{V2}(\vec{k},R) &= \frac{\vec{\omega}(\vec{k},R)}{4\pi R}.
\end{aligned} \tag{5.20}$$

At the limit $k\to 0$ we have the following expression:

$$\begin{aligned}
\omega_3(\vec{k},R)\Big|_{k\to0} &= \frac{4\pi R^3}{3},\\
\omega_2(\vec{k},R)\Big|_{k\to0} &= 4\pi R^2,\\
\omega_1(\vec{k},R)\Big|_{k\to0} &= R,\\
\omega_0(\vec{k},R)\Big|_{k\to0} &= 1,\\
\vec{\omega}_{V2}(\vec{k},R)\Big|_{k\to0} &= \vec{0},\\
\vec{\omega}_{V1}(\vec{k},R)\Big|_{k\to0} &= \vec{0}.
\end{aligned} \tag{5.21}$$

$\delta\beta\Omega_{\mathbf{ex}}^{\mathbf{MF}}/\delta\rho$

$$\frac{\delta\beta\Omega_{\mathrm{ex}}^{\mathrm{MF}}}{\delta\rho} = \frac{1}{V}\mathcal{F}^{-1}\left\{\rho(\vec{k})w(k)\right\} \tag{5.22}$$

$\partial\Omega_{\mathbf{ex}}^{\mathbf{HS}}/\partial h_m$

In this section, we need to optimize the period of phases. The optimization of box size is associated to the calculation of $\frac{\delta\Omega}{\delta h_m}$. Similar to Eq. (5.10), $\partial\Omega_{\mathrm{ex}}^{\mathrm{HS}}/\partial h_m$ can be written as,

$$\begin{aligned}\frac{\partial\Omega_{\mathrm{ex}}^{\mathrm{HS}}[n_l(\vec{r}_1)]}{\partial h_m} =& \sum_l \int d\vec{r}_2 \frac{\delta\Omega_{\mathrm{ex}}^{\mathrm{HS}}[n_l(\vec{r}_1)]}{\delta n_l(\vec{r}_2)} \frac{\partial n_l(\vec{r}_2)}{\partial h_m} \\ =& \frac{1}{V}\sum_l \int d\vec{r}_2 T_l(\vec{r}_2) \frac{\partial n_l(\vec{r}_2)}{\partial h_m}.\end{aligned} \tag{5.23}$$

where $T_l(\vec{r}_2)$ are the same as before and $\frac{\partial n_l(\vec{r}_2)}{\partial h_m}$ are computed via,

$$\frac{\partial n_l(\vec{r}_2)}{\partial h_m} = \mathcal{F}^{-1}\left\{\rho(\vec{k})\frac{\partial\omega_l(k)}{\partial h_m}\right\}. \tag{5.24}$$

$\frac{\partial\omega_l(k)}{\partial h_m}$ are given by,

$$\begin{aligned}
\frac{\partial\omega_3(\vec{k},R)}{\partial h_m} =& \frac{\partial\omega_3(\vec{k},R)}{\partial k}\left(-\frac{1}{h_m}\frac{k_m^2}{k}\right),\\
\frac{\partial\omega_2(\vec{k},R)}{\partial h_m} =& \frac{\partial\omega_2(\vec{k},R)}{\partial k}\left(-\frac{1}{h_m}\frac{k_m^2}{k}\right),\\
\frac{\partial\omega_1(\vec{k},R)}{\partial h_m} =& \frac{\partial\omega_1(\vec{k},R)}{\partial k}\left(-\frac{1}{h_m}\frac{k_m^2}{k}\right),\\
\frac{\partial\omega_0(\vec{k},R)}{\partial h_m} =& \frac{\partial\omega_0(\vec{k},R)}{\partial k}\left(-\frac{1}{h_m}\frac{k_m^2}{k}\right).
\end{aligned} \tag{5.25}$$

$$\frac{\partial\left[\omega_{V2}(\vec{k},R)\right]_n}{\partial h_m} = \begin{cases} i\dfrac{k_m}{h_m}\left[\omega_3(\vec{k},R)+\dfrac{k_m^2}{k}\dfrac{\partial\omega_3(\vec{k},R)}{\partial k}\right], & m=n \\ ik_n\dfrac{1}{h_m}\dfrac{k_m^2}{k}\dfrac{\partial\omega_3(\vec{k},R)}{\partial k}, & m\neq n \end{cases} \tag{5.26}$$

$$\frac{\partial\vec{\omega}_{V1}(\vec{k},R)}{\partial h_m} = \frac{\partial\vec{\omega}_{V2}(\vec{k},R)}{\partial h_m}\Big/ 4\pi R, \tag{5.27}$$

where $\left[\omega_{V2}(\vec{k},R)\right]_n$ denotes the n^{th} component of $\vec{\omega}_{V2}(\vec{k},R)$. And the explicit expressions are listed below:

$$\begin{aligned}
\frac{\partial\omega_3(\vec{k},R)}{\partial k} =& \frac{4\pi\left[3kR\cos(kR)+(-3+k^2R^2)\sin(kR)\right]}{k^4},\\
\frac{\partial\omega_2(\vec{k},R)}{\partial k} =& \frac{4\pi R\left[kR\cos(kR)-\sin(kR)\right]}{k^2},\\
\frac{\partial\omega_1(\vec{k},R)}{\partial k} =& \frac{\left[kR\cos(kR)-\sin(kR)\right]}{k^2},\\
\frac{\partial\omega_0(\vec{k},R)}{\partial k} =& \frac{\left[kR\cos(kR)-\sin(kR)\right]}{k^2R},
\end{aligned} \tag{5.28}$$

with,

$$\left.\frac{\partial\omega_3(\vec{k},R)}{\partial k}\right|_{k\to 0} = \left.\frac{\partial\omega_2(\vec{k},R)}{\partial k}\right|_{k\to 0} = \left.\frac{\partial\omega_1(\vec{k},R)}{\partial k}\right|_{k\to 0} = \left.\frac{\partial\omega_0(\vec{k},R)}{\partial k}\right|_{k\to 0} = 0. \quad (5.29)$$

Summary of minimization process

For the lattice gas model and LDA model, the minimization procedure of preconditioned conjugated gradient method is summarized below.

1. **Initialization**. Input the initial guess of ρ and obtain $\rho(k)$ and $\eta(r)$. At the first step, there is no history of $\psi(r)$ and $\xi(r)$, so $\zeta^1 = 0$.

2. **Computing preconditioner**. In order to obtain $\xi^i(\vec{r})$, we need to calcualte quantities: $\frac{\delta\beta\Omega}{\delta\rho}$ and $\delta^2\beta\Omega/\delta\rho^2$

3. **CGD Preparation**. Update $\psi^i(\vec{r})$ and perform the Fourier transform to get $\psi^i(\vec{k})$.

4. **Store History**. Store $\xi^i(\vec{r})$ and $\psi^i(\vec{r})$ for the next step.

5. **Adapt Step Size**. Compute ϵ^i and θ^i. Required quantities: $\frac{\delta\Omega}{\delta\rho(\vec{r})}$ (computed already), $\frac{\partial^2 g^i}{\partial\epsilon^2}$, $\frac{dw(k)}{dk}$, $\frac{dk}{dh_l} \to \frac{\partial\Omega}{\partial h_l}$ (3 for 3D), $\frac{d^2w(k)}{dk^2}$, $\frac{d^2k}{dh_l dh_{l'}}$, $\to \frac{\partial^2\Omega}{\partial h_l \partial h_{l'}}$ (9 for 3D). In practice, we have found that ϵ and θ sometimes become negative. In that case, we flip their sign to maintain positive values. We have also found that the magnitude of ϵ may sometimes be quite large leading to divergence. To solve this problem, we use a manual line search where we store the value of $\max\left(\left|\frac{\delta F}{\delta\rho}\right|\right)$ for step i and iteratively decrease ϵ via $\epsilon = 0.9 * \epsilon$ until $\max\left(\left|\frac{\delta F}{\delta\rho}\right|_{i+1}\right) < \max\left(\left|\frac{\delta F}{\delta\rho}\right|_i\right)$ or ϵ is lower than some threshold (a small value such as 0.01 times the original ϵ). The spirit is that we only take a large step if it leads to a point

with smaller absolute gradient, otherwise we just take a smaller step instead unless the step becomes too small. The line search procedure can help us to determine a step size that has a reasonable trade off between faster convergence and better stability.

6. **Execute GD or CGD**. Update the fields and periods. If $\rho(\vec{r})$ becomes negative, assign it to a small positive value, e.g. 10^{-8}. If the periods become negative, we flip their sign.

7. **Update all quantities**. Update $\rho(\vec{k})$, $\eta(\vec{r})$ as well as all quantities that depend on the periods.

8. **Calculate the Grand Potential**. Compute the grand potential.

9. **Judge Convergence**. Judge if the converging criteria are satisfied: Yes → output the results; No → come back to step 2 and repeat steps 2 to 9 until convergence.

For the FMT-WB, we perform the simple mixing and Anderson mixing algorithm:

1. **Initialization**. Input the initial guess of ρ and obtain $\rho(k)$

2. **Weight functions and weighted densities**. At this step, we compute $\omega_\alpha(k)$ and $n_\alpha(k)$. $n_\alpha(k) \rightarrow n_\alpha(r)$. Then we compute $T_l(r)$, $T_l(k)$ and obtain $\delta\beta\Omega_{ex}^{HS}/\delta\rho$.

3. **Grand potential**. We also need to calculate $\omega(k)$ and use the quantities obtained previously to calculate the grand potential. Calculate the potential energy difference $\Delta\Omega$: $\Omega_{new} - \Omega_{old}$.

4. **Compute new** ρ. Compute $\delta\Omega_{ex}^{HS}/\delta\rho$, $\delta\Omega_{ex}^{MF}/\delta\rho$ to obtain ρ_{new}. Compute $\rho_{\textbf{diff}} = \rho_{\text{new}} - \rho$. Find the maximum value of ρ_{diff} and set it to be the error.

5. **Compute** $h^{\textbf{new}}$. Calculate quantities $\delta(\beta\Omega)/\delta h_m$ and new periods: $h_m^{\text{new}} = h_m - \delta\beta\Omega/\delta h_m$. Find the maximum value of $d\beta\Omega/dh_m$ and set it to be dh_{max}.

6. **Store history** Store the history of ρ_{diff} and ρ_{new}.

7. **Update** ρ **and periods** If $|error| > 10^{-5}$, we perform the simple mixing method: $\rho^{i+1} = \rho^i + \alpha\rho^{\text{new}}$ and $h_m^{i+1} = h_m^i - \alpha d(\beta\Omega)/dh_m$. Otherwise, we perform the Anderson mixing method.

8. **Judge Convergence** Using three conditions to judge the convergence: $|\Delta\Omega| < 10^{-10}$, $|error| < 10^{-7}$, $dh_{\text{max}} < 10^{-7}$. If three conditions are satisfied, we terminate the iteration and output the results. Otherwise, repeat step (2) to step (7).

5.2 Appendix B

Phase initialization

We list our initial phases configurations in the table below. Those initial phases are used as initial input in lattice gas model and local density approximation. Then we use 1 to subtract the density function of phases. For example we can get the initial density profile of inverse BCC phase via: $\rho^{INVBCC}(x, y, z) = 1 - \rho^{BCC}(x, y, z)$. In the table, L_0 is the distance between nearest neighbour cluster. The period of each phase is calculated from the geometric relationship. For FMT-WB, directly using those initial complex phases (i.e. A15 and σ) as initial conditions complex might

cause instability issue during the iteration process. One proper way to solve this problem is to use convergent solutions obtained from local density approximation as initial input.

Initial phase configurations			
phase	discretization size	Unit cell dimensions	initial functions or configurations
BCC	$N_x = 64$ $N_y = 64$ $N_z = 64$	$L_x = \sqrt{2}L_0$ $L_y = \sqrt{2}L_0$ $L_z = \sqrt{2}L_0$	(0,0,1),(0,1,0) (1,0,0),(1,1,0) (1,0,1),(1,1,1) (0,1,1),(0,0,0) $(\frac{1}{2},\frac{1}{2},\frac{1}{2})$
FCC	$N_x = 64$ $N_y = 64$ $N_z = 64$	$L_x = \sqrt{3}L_0$ $L_y = \sqrt{3}L_0$ $L_z = \sqrt{3}L_0$	(0,0,1),(0,1,0) (1,0,0),(1,1,0) (1,0,1),(1,1,1) (0,1,1),(0,0,0) $(\frac{1}{2},\frac{1}{2},0)$,$(\frac{1}{2},\frac{1}{2},1)$ $(0,\frac{1}{2},\frac{1}{2})$,$(\frac{1}{2},0,\frac{1}{2})$ $(\frac{1}{2},1,\frac{1}{2})$,$(1,\frac{1}{2},\frac{1}{2})$
HCP	$N_x = 64$ $N_y = 64$ $N_z = 64$	$L_x = 1.31L_0$ $L_y = 2.27L_0$ $L_z = 2.09L_0$	(0.5,0.1667,0.5),(0,0.6667,0.5) (1,0.6667,0.5),(1,0.6667,0.5) (0,0,0),(1,0,1) (0,1,0),(0,0,1) $(1,1,0)$,$(1,0,0)$ $(0,1,1)$,$(1,1,1)$

			(0.5, 0.5, 0),(0.5, 0.5, 1)
A15	$N_x = 96$ $N_y = 96$ $N_z = 96$	$L_x = 2.31L_0$ $L_y = 2.31L_0$ $L_z = 2.31L_0$	(0,0,0),(1,0,0) (0,1,0),(0,0,1) (1,1,0),(1,0,1) (0,1,1),(1,1,1) (0.5, 0.5, 0.5),(0.75, 1, 0.5) (0.25, 1, 0.5),(0.5, 0.75, 0) (0.5, 0.25, 0),(1, 0.5, 0.25) (0, 0.5, 0.25),(1, 0.5, 0.75) (0, 0.5, 0.75),(0.5, 0.75, 1) (0.5, 0.25, 1),(0.75, 0, 0.5) (0.25, 0, 0.5)
σ	$N_x = 96$ $N_y = 96$ $N_z = 96$	$L_x = 2.31L_0$ $L_y = 2.31L_0$ $L_z = 2.31L_0$	(0,0,0),(0.3177, 0.6823, 0.2476) (0,1,0),(0.8177, 0.8177, 0.7476) (1,1,0),(0.6823, 0.3177, 0.2476) (0,1,1),(0.1823, 0.1823, 0.2524) (0.5, 0.5, 0.5),(0.3684, 0.9632, 0.5) (0.5368, 0.8684, 0),(0.5368, 0.8684, 1) (0.8684, 0.5368, 0),(0.9632, 0.3684, 0.5) (0.8684, 0.5368, 1),(0.0368, 0.6316, 0.5) (0.1316, 0.4632, 1),(0.1316, 0.4632, 0) (0.4632, 0.1316, 0),(0.6316, 0.0368, 0.5) (0.4632, 0.1316, 1) (0.3177, 0.6823, 0.7524), (1, 0, 0) (0.8177, 0.8177, 0.2524), (0, 0, 1)

			$(0.6823, 0.3177, 0.7524), (1, 0, 1)$ $(0.1823, 0.1823, 0.7476), (1, 1, 1)$ $(0.1019, 0.8981, 0.5), (0.6019, 0.6019, 1)$ $(0.6019, 0.6019, 0), (0.3981, 0.3981, 1)$ $(0.3981, 0.3981, 0), (0.8981, 0.1019, 0.5)$ $(0.0653, 0.7376, 0), (0.0653, 0.7376, 1)$ $(0.2624, 0.9347, 0), (0.2624, 0.9347, 1)$ $(0.5653, 0.7624, 0.5), (0.2376, 0.4347, 0.5)$ $(0.7624, 0.5653, 0.5), (0.4347, 0.2376, 0.5)$ $(0.7376, 0.0653, 0), (0.7376, 0.0653, 1)$ $(0.9347, 0.2624, 0), (0.9347, 0.2624, 1)$
HEX	$N_x = 128$ $N_y = 128$ $N_z = 16$	$L_x = 1.17L_0$ $L_y = \sqrt{3}L_0$ $L_z = L_0$	$\rho(x, y, z) = \cos(4\pi y/L_y) + 2\cos(2\pi x/L_x)\cos(2\pi y/L_y)$
Lam	$N_x = 128$ $N_y = 16$ $N_z = 16$	$L_x = L_0$ $L_y = L_0$ $L_z = L_0$	$\rho(x, y, z) = 1.0 + 0.5\cos(2\pi x/L_x)$
DG	$N_x = 64$	$L_x = 2.5L_0$	$\rho(x, y, z) = \sqrt{8.0/3.0}(\cos(x)\sin(2y)\sin(z) + \cos(y)\sin(z)\sin(2x) + \cos(z)\sin(x)\sin(2y)) + 1.0/\sqrt{3}((\cos(2(x + y)) + \cos(2(x - y)) + \cos(2(z + y)) + \cos(2(y - z)) + \cos(2 * (x + z)) + \cos(2 * (x - z))))$

	$N_y = 64$ $N_z = 64$	$L_y = 2.5L_0$ $L_z = 2.5L_0$	

TABLE 5.1: The phase initialization parameters used in our works.

5.3 Appendix C

The density profiles of FMT-WB model

We plot the converged density profiles for following phases: HCP, Double Gyroid, Lamella, σ and A15 in Figure (5.1).

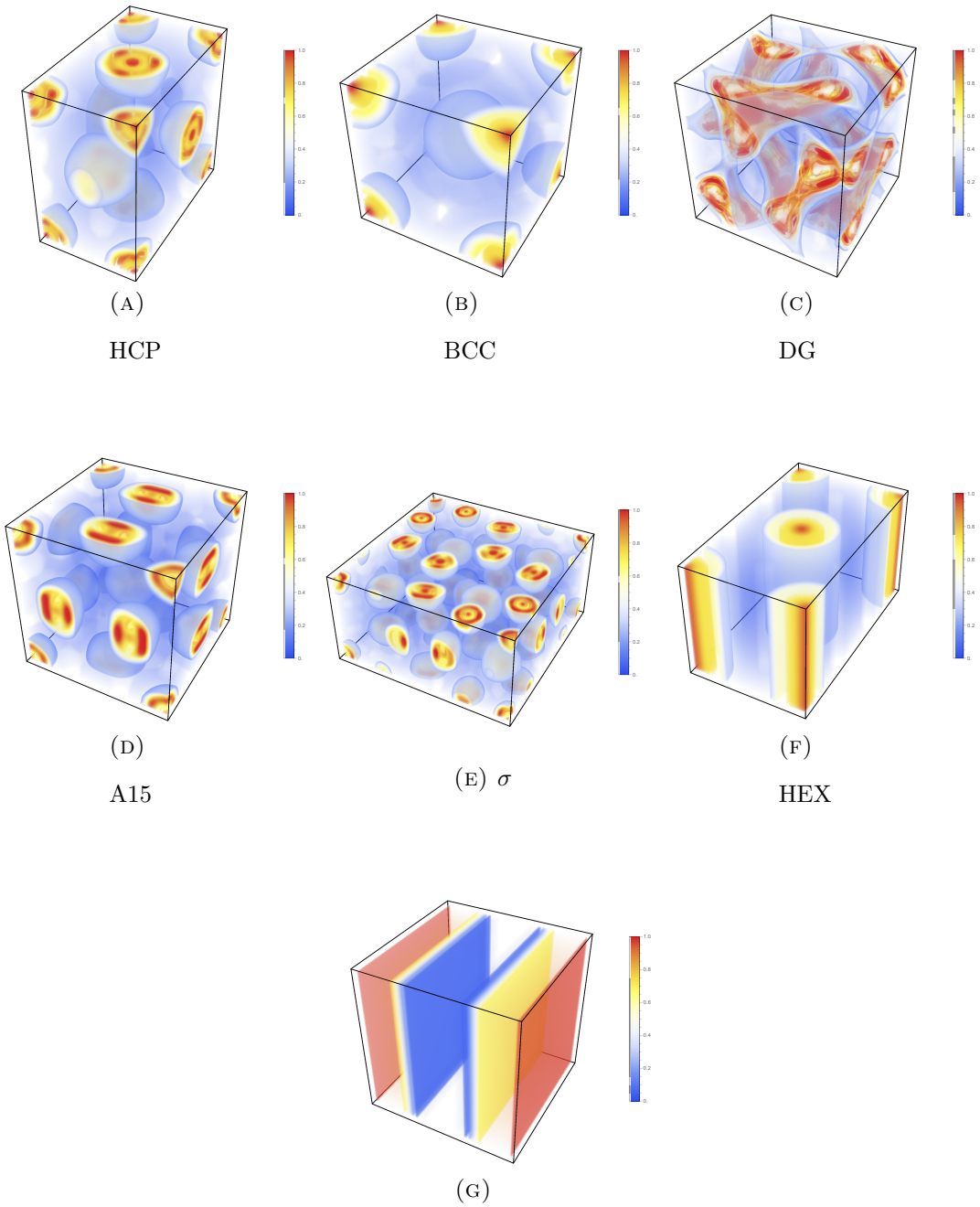

(A) HCP (B) BCC (C) DG

(D) A15 (E) σ (F) HEX

(G) Lamella

FIGURE 5.1: Three-dimensional density profiles of different phases are generated by FMT-WB model. The local packing effect is clearly visible within clusters of spherical phases.

Bibliography

[1] AJ Archer. "Density functional theory for the freezing of soft-core fluids". In: *Physical Review E* 72.5 (2005), p. 051501.

[2] Carlos M Baez-Cotto and Mahesh K Mahanthappa. "Micellar mimicry of intermetallic C14 and C15 laves phases by aqueous lyotropic self-assembly". In: *ACS nano* 12.4 (2018), pp. 3226–3234.

[3] VSK Balagurusamy et al. "Rational design of the first spherical supramolecular dendrimers self-organized in a novel thermotropic cubic liquid-crystalline phase and the determination of their shape by X-ray analysis". In: *Journal of the American Chemical Society* 119.7 (1997), pp. 1539–1555.

[4] Vasili Baranau and Ulrich Tallarek. "Random-close packing limits for monodisperse and polydisperse hard spheres". In: *Soft Matter* 10.21 (2014), pp. 3826–3841.

[5] Norman F Carnahan and Kenneth E Starling. "Equation of state for nonattracting rigid spheres". In: *The Journal of chemical physics* 51.2 (1969), pp. 635–636.

[6] José A Cuesta and Yuri Martınez-Ratón. "Fundamental measure theory for mixtures of parallel hard cubes. I. General formalism". In: *The Journal of chemical physics* 107.16 (1997), pp. 6379–6389.

[7] Sarah Dawson. "Ginzburg-Landau theory of complex spherical packing phases in soft condensed matter". PhD thesis. 2021.

[8] Markus Edelmann and Roland Roth. "Gyroid phase of fluids with spherically symmetric competing interactions". In: *Physical Review E* 93.6 (2016), p. 062146.

[9] Frederick C Frank and John S Kasper. "Complex alloy structures regarded as sphere packings. I. Definitions and basic principles". In: *Acta Crystallographica* 11.3 (1958), pp. 184–190.

[10] Stéphanie Hajiw, Brigitte Pansu, and Jean-François Sadoc. "Evidence for a C14 Frank–Kasper phase in one-size gold nanoparticle superlattices". In: *ACS nano* 9.8 (2015), pp. 8116–8121.

[11] Jean-Pierre Hansen and Ian Ranald McDonald. *Theory of simple liquids: with applications to soft matter*. Academic press, 2013.

[12] Hendrik Hansen-Goos and Roland Roth. "Density functional theory for hard-sphere mixtures: the White Bear version mark II". In: *Journal of Physics: Condensed Matter* 18.37 (2006), p. 8413.

[13] A Imperio and L Reatto. "Microphase separation in two-dimensional systems with competing interactions". In: *The Journal of chemical physics* 124.16 (2006), p. 164712.

[14] C.Burns J.Xie and An-Chang Shi. "Complex spherical packing phases formed in hard sphere cluster crystals". In: *unpublished* (2021).

[15] E Kierlik and ML Rosinberg. "Free-energy density functional for the inhomogeneous hard-sphere fluid: Application to interfacial adsorption". In: *Physical review A* 42.6 (1990), p. 3382.

[16] Kyungtae Kim et al. “Origins of low-symmetry phases in asymmetric diblock copolymer melts”. In: *Proceedings of the National Academy of Sciences* 115.5 (2018), pp. 847–854.

[17] Sung A Kim et al. “Low-symmetry sphere packings of simple surfactant micelles induced by ionic sphericity”. In: *Proceedings of the National Academy of Sciences* 114.16 (2017), pp. 4072–4077.

[18] Sangwoo Lee, Michael J Bluemle, and Frank S Bates. “Discovery of a Frank-Kasper σ phase in sphere-forming block copolymer melts”. In: *Science* 330.6002 (2010), pp. 349–353.

[19] Sangwoo Lee, Chris Leighton, and Frank S Bates. “Sphericity and symmetry breaking in the formation of Frank–Kasper phases from one component materials”. In: *Proceedings of the National Academy of Sciences* 111.50 (2014), pp. 17723–17731.

[20] Christos N Likos et al. “Why do ultrasoft repulsive particles cluster and crystallize? Analytical results from density-functional theory”. In: *The Journal of chemical physics* 126.22 (2007), p. 224502.

[21] CN Likos. “Colloidal interactions: From effective potentials to structure”. In: *La Rivista del Nuovo Cimento* 37 (2014), pp. 125–180.

[22] Aaron P Lindsay et al. “A15, σ, and a quasicrystal: Access to complex particle packings via bidisperse diblock copolymer blends”. In: *ACS Macro Letters* 9.2 (2020), pp. 197–203.

[23] Meijiao Liu et al. “Stabilizing the Frank-Kasper phases via binary blends of AB diblock copolymers”. In: *ACS Macro Letters* 5.10 (2016), pp. 1167–1171.

[24] James F Lutsko. "Recent developments in classical density functional theory". In: *Advances in chemical physics* 144 (2010), p. 1.

[25] GA Mansoori et al. "Equilibrium thermodynamic properties of the mixture of hard spheres". In: *The Journal of Chemical Physics* 54.4 (1971), pp. 1523–1525.

[26] Mark W Matsen. "The standard Gaussian model for block copolymer melts". In: *Journal of Physics: Condensed Matter* 14.2 (2001), R21.

[27] Duncan McClenagan. "Landau theory of complex ordered phases". PhD thesis. 2019.

[28] Leandro Missoni and Mario Tagliazucchi. "Body centered tetragonal nanoparticle superlattices: why and when they form?" In: *Nanoscale* 13.34 (2021), pp. 14371–14381.

[29] Bianca M Mladek et al. "Formation of polymorphic cluster phases for a class of models of purely repulsive soft spheres". In: *Physical review letters* 96.4 (2006), p. 045701.

[30] Roderich Moessner and Arthur P Ramirez. "Geometrical frustration". In: *Physics Today* 59.2 (2006), pp. 24–29.

[31] Peter D Olmsted and Scott T Milner. "Strong-segregation theory of bicontinuous phases in block copolymers". In: *Physical review letters* 72.6 (1994), p. 936.

[32] Peter D Olmsted and Scott T Milner. "Strong segregation theory of bicontinuous phases in block copolymers". In: *Macromolecules* 31.12 (1998), pp. 4011–4022.

[33] Gunja Pandav, Victor Pryamitsyn, and Venkat Ganesan. "Interactions and aggregation of charged nanoparticles in uncharged polymer solutions". In: *Langmuir* 31.45 (2015), pp. 12328–12338.

[34] Brigitte Pansu et al. "Softness-driven complexity in supercrystals of gold nanoparticles". In: *Soft Matter* 17.26 (2021), pp. 6461–6469.

[35] Jerome K Percus and George J Yevick. "Analysis of classical statistical mechanics by means of collective coordinates". In: *Physical Review* 110.1 (1958), p. 1.

[36] JK Percus. "Equilibrium state of a classical fluid of hard rods in an external field". In: *Journal of Statistical Physics* 15.6 (1976), pp. 505–511.

[37] Davide Pini. "Some general features of mesophase formation in hard-core plus tail potentials". In: *Soft Matter* 14.31 (2018), pp. 6595–6612.

[38] Davide Pini and Alberto Parola. "Pattern formation and self-assembly driven by competing interactions". In: *Soft Matter* 13.48 (2017), pp. 9259–9272.

[39] Davide Pini, Alberto Parola, and Luciano Reatto. "An unconstrained DFT approach to microphase formation and application to binary Gaussian mixtures". In: *The Journal of Chemical Physics* 143.3 (2015), p. 034902.

[40] Abhiram Reddy and Gregory M Grason. "A cornerstone of complex crystals". In: *Nature Chemistry* 11.10 (2019), pp. 865–867.

[41] Abhiram Reddy et al. "Stable Frank–Kasper phases of self-assembled, soft matter spheres". In: *Proceedings of the National Academy of Sciences* 115.41 (2018), pp. 10233–10238.

[42] Y Rosenfeld et al. "Fundamental-measure free-energy density functional for hard spheres: Dimensional crossover and freezing". In: *Physical Review E* 55.4 (1997), p. 4245.

[43] Yaakov Rosenfeld. "Free-energy model for the inhomogeneous hard-sphere fluid mixture and density-functional theory of freezing". In: *Physical review letters* 63.9 (1989), p. 980.

[44] Roland Roth. "Fundamental measure theory for hard-sphere mixtures: a review". In: *Journal of Physics: Condensed Matter* 22.6 (2010), p. 063102.

[45] Roland Roth et al. "Fundamental measure theory for hard-sphere mixtures revisited: the White Bear version". In: *Journal of Physics: Condensed Matter* 14.46 (2002), p. 12063.

[46] Jean-François Sadoc and Rémy Mosseri. "Quasiperiodic Frank–Kasper phases derived from the square–triangle dodecagonal tiling". In: *Structural Chemistry* 28.1 (2017), pp. 63–73.

[47] P Schiffer and AP Ramirez. "Recent experimental progress in the study of geometrical magnetic frustration". In: *Comments on Condensed Matter Physics* 18.1 (1996), pp. 21–50.

[48] An-Chang Shi. "Frustration in block copolymer assemblies". In: *Journal of Physics: Condensed Matter* 33.25 (2021), p. 253001.

[49] Homin Shin, Gregory M Grason, and Christian D Santangelo. "Mesophases of soft-sphere aggregates". In: *Soft Matter* 5.19 (2009), pp. 3629–3638.

[50] Pawel Stasiak and MW Matsen. "Efficiency of pseudo-spectral algorithms with Anderson mixing for the SCFT of periodic block-copolymer phases". In: *The European Physical Journal E* 34.10 (2011), pp. 1–9.

[51] Zebin Su, Mingjun Huang, and Stephen ZD Cheng. "Complex self-assembled lattices from simple polymer blends". In: *Proceedings of the National Academy of Sciences* 117.33 (2020), pp. 19618–19620.

[52] P Tarazona. "Density functional for hard sphere crystals: A fundamental measure approach". In: *Physical Review Letters* 84.4 (2000), p. 694.

[53] Russell B Thompson, K O/ Rasmussen, and Turab Lookman. "Improved convergence in block copolymer self-consistent field theory by Anderson mixing". In: *The Journal of chemical physics* 120.1 (2004), pp. 31–34.

[54] Denis Weaire and Robert Phelan. "A counter-example to Kelvin's conjecture on minimal surfaces". In: *Philosophical Magazine Letters* 69.2 (1994), pp. 107–110.

[55] Jianzhong Wu. *Variational Methods in Molecular Modeling*. Springer, 2016.

[56] Jiayu Xie, Yu Li, and An-Chang Shi. "Binary blends of diblock copolymers: An efficient route to complex spherical packing phases". In: *Macromolecular Theory and Simulations* 30.6 (2021), p. 2100053.

[57] Jiayu Xie and An-Chang Shi. "Formation of complex spherical packing phases in diblock copolymer/homopolymer blends". In: *Giant* 5 (2021), p. 100043.

[58] Nan Xie et al. "σ phase formed in conformationally asymmetric AB-type block copolymers". In: *Acs Macro Letters* 3.9 (2014), pp. 906–910.

[59] Mohammad Hossein Yamani. "Colloidal hard sphere crystals and their interfaces in density functional theory". PhD thesis. Universitätsbibliothek Tübingen, 2014.

[60] X-M You, A Yu Vlasov, and AJ Masters. "The equation of state of isotropic fluids of hard convex bodies from a high-level virial expansion". In: *The Journal of chemical physics* 123.3 (2005), p. 034510.

[61] Yang-Xin Yu and Jianzhong Wu. "Structures of hard-sphere fluids from a modified fundamental-measure theory". In: *The Journal of chemical physics* 117.22 (2002), pp. 10156–10164.

[62] Xiangbing Zeng et al. "Supramolecular dendritic liquid quasicrystals". In: *Nature* 428.6979 (2004), pp. 157–160.

[63] Mingtian Zhao and Weihua Li. "Laves phases formed in the binary blend of AB4 miktoarm star copolymer and A-homopolymer". In: *Macromolecules* 52.4 (2019), pp. 1832–1842.